

CHALMERS



Aerodynamic Analysis of wind turbine

Master's thesis in Fluid Mechanics

AYYOOB ZARMEHRI

Department of Applied Mechanics

Division of Fluid dynamics

CHALMERS UNIVERSITY OF TECHNOLOGY

Gothenburg, Sweden 2012

Master's thesis 2012:58

MASTER'S THESIS IN FLUID MECHANICS

Aerodynamic Analysis of wind turbine

AYYOOB ZARMEHRI

Department of Applied Mechanics
Division of Fluid dynamics
CHALMERS UNIVERSITY OF TECHNOLOGY
Gothenburg, Sweden 2012

Aerodynamic Analysis of wind turbine
AYYOOB ZARMEHRI

© AYYOOB ZARMEHRI, 2012

Master's thesis 2012:58
ISSN 1652-8557
Department of Applied Mechanics
Division of Fluid dynamics
Chalmers University of Technology
SE-412 96 Gothenburg
Sweden
Telephone: +46 (0)31-772 1000

Chalmers Reproservice
Gothenburg, Sweden 2012

Aerodynamic Analysis of wind turbine
Master's thesis in Fluid Mechanics
AYYOOB ZARMEHRI
Department of Applied Mechanics
Division of Fluid dynamics
Chalmers University of Technology

ABSTRACT

The thesis investigates the application of vortex theory for analyzing the aerodynamic loads on wind turbine blades. Based on this method, a graphical user friendly program is developed to be used by the industry. The method, however, requires airfoil data of each section of the blade geometry. To this end, a newly published transitional turbulence model and a variation of Explicit Algebraic Reynolds stress models (EARSM) are implemented into the CALC-BFC CFD solver and their potential for calculating airfoil characteristics are studied and compared to the XFOIL program. A hyperbolic mesh generation program is also developed to provide high quality grids for CFD simulations. The overall performance of the method is evaluated against a full 3D CFD analysis by ANSYS-CFX solver.

Keywords: Incompressible Flow, Wind Turbine, Lifting Line Theory, Hyperbolic mesh generation, EARSM, transition modeling

ACKNOWLEDGEMENT

The thesis work has been conducted at Chalmers University of Technology, department of applied mechanics, division of Fluid dynamics with the support and collaboration of Semcon AB, Sweden.

It's a great pleasure to thank everyone who helped me accomplish the thesis. I am truly indebted and thankful to my supervisor, Professor Lars Davidson, whose help, stimulating suggestions and encouragement was a great source of energy in all the time of my research.

I would also like to thank Lennart Berghult at Semcon AB, my friends Hamidreza Abedi and Maryam Mirzaee for all their advices and discussions we had during the work.

Last but not the least, my deepest gratitude goes to my parents, Fatemeh and Hossein, for their spiritual support through my life.

Ayyoob Zarmehri
Gothenburg, December 2012

CONTENTS

Abstract	i
Acknowledgement	iii
Contents	v
1 Introduction	1
2 CFD	2
2.1 Governing equations of fluid mechanics	2
3 Inviscid flow	4
3.1 Inviscid flow	4
4 Potential flow	6
4.1 Irrotational flow	6
4.2 Finite wing: The lifting line model	7
4.2.1 Helical vortex theory for wind turbine	9
4.2.2 Numerical procedure	9
5 Hyperbolic Grid Generation	12
6 Turbulence Modeling	15
6.1 Linear Eddy-Viscosity Models	15
6.1.1 The $k - \varepsilon$ model	16
6.1.2 The $k - \omega$ model	17
6.1.3 The $k - \omega$ SST model	17
6.2 Non-Linear Eddy-Viscosity Models	19
6.2.1 Explicit Algebraic Reynolds Stress Model formulation	19
6.2.2 EARSM-BSL- $k - \omega$	22
6.2.3 EARSM-AKN- $k - \varepsilon$	23
6.3 Transitional Turbulence Modeling	23
6.3.1 Transitional turbulent $k - \omega$ SST model	23
7 Results and discussions	27
7.1 Lifting line method	27
7.2 Flat plate test cases	29
7.2.1 $\gamma - \tilde{Re}_\theta$ model	30
7.2.2 EARSM model	32
7.3 XFOIL program	33
7.4 Airfoils 2D simulations	33
7.4.1 $\gamma - \tilde{Re}_\theta$ model	33
7.4.2 EARSM model	35
7.5 3D steady-state CFD simulation	35
8 Conclusion	39

1 Introduction

Wind turbine technology is considered one of the most promising areas of renewable energy sources. Most importantly, wind turbine operation does not emit any green house gases. However, the manufacturing and installation of wind turbines are quite costly and produce pollutants. Furthermore, wind turbines are subject to different and sometimes unknown types of aerodynamic loadings in their life time operation. This study is aimed at a better understanding of aerodynamic loads on the wind turbine blades, providing a fast engineering tool for analysing and designing the blade.

From the design point of view, in which a designer starts from the scratch, the designing tool should have certain characteristics. First of all it should be fast enough to help the designer explore thousands of different configurations within a short time. Secondly, it is preferable that the tool has the ability to guide the designer towards the best and optimum solution, rather than randomly trying different configurations.

In the following chapters, two methods, namely computational fluid dynamics (CFD) and potential flow theory, are presented and their characteristics are evaluated against the criteria mentioned above.

2 CFD

2.1 Governing equations of fluid mechanics

By applying the conservation laws of physics to a fluid element, one can formulate the equations describing the motion of the fluid element. These laws are conservation of mass, linear and angular momentum and energy. By combining these equations with continuum hypothesis and the assumption of isotropic Newtonian fluids, the so-called Navier-Stokes equations can be derived. These equations make a system of four partial differential equations for the pressure and the three components of velocity vector. In tensor notation Navier-Stokes equations for incompressible flows with constant viscosity and no body force read as:

$$\frac{\partial v_i}{\partial x_i} = 0 \quad (2.1.1)$$

$$\rho \frac{\partial v_i}{\partial t} + \rho \frac{\partial v_i v_j}{\partial x_j} = -\frac{\partial p}{\partial x_i} + \mu \frac{\partial^2 v_i}{\partial x_j \partial x_j} \quad (2.1.2)$$

The exact solution to these equations is generally extremely difficult and few such solutions exist only for some simple flows [7]. The difficulty arises due to the nonlinearity of these equations, which makes the use of principle of superpositions impossible. This nonlinear nature of these equations can lead to bifurcation and chaos in the solution, making the solution non-unique for the given initial and boundary conditions [7]. One such bifurcation is the laminar to turbulent transition causing chaotic structures in the flow. This normally happens at large Reynolds number where the fluid inertia overcomes viscous forces and laminar flow loses its stability and transition to turbulence takes place. A turbulent flow is always unsteady and three dimensional.

With the advent of fast computers and advances in numerical methods, the trend nowadays is towards the numerical simulation of Navier-Stokes equations. For numerical simulation, one solves the discretized version of these equations in a domain. This field is known as Computational Fluid Dynamics (CFD). In CFD, differential equations are *approximated* by a system of algebraic equations through a process known as *discretization*. The algebraic equations can then be solved on a computer. The discretization is carried out both in time and space. For spatial discretization, a computational mesh needs to be generated in the domain of interest. Mesh generation is the first and the most important step in CFD calculations and the results are heavily dependent on the quality of the mesh. Mesh generation is presented in chapter 5 of this thesis and one good algorithm for mesh generation for external aerodynamic applications is presented.

It should be emphasized here again that numerical simulation is in fact an approximation of the real physics. Assuming that the differential equations represent the real physics, one can talk about the accuracy level of the numerical simulation. In theory, a solution with any desired accuracy is achievable. In order to achieve accurate numerical solution, the computational mesh and the time step should be fine enough to capture the smallest structures of the flow. This is the topic of Direct Numerical Simulation (DNS). Unfortunately the computational cost of DNS is so expensive that even with super computers it is only applicable for flows with low Reynolds number.

Hopefully, for many engineering applications the accuracy level of the solution doesn't need to be the same as it is in DNS and less accurate solutions with lower computational costs are acceptable.

In Large Eddy Simulation (LES), the larger structures of the flow that can be resolved by the mesh are solved while the ones smaller than the mesh are modeled [5]. Although LES has proven to give accurate and acceptable results for engineering applications, the range of applicability of this method is heavily influenced by its computational time. For wind turbine applications, LES has been used mainly for wake interactions of wind turbines in wind parks.

For many engineering applications, where the simulation time is of primary concern and a complete time history of every aspect of a turbulent flow is not needed, engineers are only interested in the time-averaged version of Navier-Stokes equations. The time averaged Navier-Stokes equations for incompressible flows read as [5]:

$$\frac{\partial \bar{v}_i}{\partial x_i} = 0 \quad (2.1.3)$$

$$\rho \frac{\partial \bar{v}_i}{\partial t} + \rho \frac{\partial \bar{v}_i \bar{v}_j}{\partial x_j} = -\frac{\partial \bar{p}}{\partial x_i} + \frac{\partial}{\partial x_j} \left(\mu \frac{\partial \bar{v}_i}{\partial x_j} - \overline{\rho v'_i v'_j} \right) \quad (2.1.4)$$

where the additional term $-\overline{\rho v'_i v'_j}$ is called Reynolds Stress, which is the result of time averaging and stems from fluctuating velocity field (turbulence) [5]. In order to solve these equations, the unknown Reynolds stresses need to be modeled. Although the time averaged equations are much less expensive to solve compared to LES, modeling of Reynolds stresses introduces modeling error to the final solution. This is the subject of turbulence modeling which is discussed in chapter 6.

Usually two-equation models are used for turbulence modeling. Laminar-turbulent transition also needs to be addressed. A two-equation transition modeling is presented in chapter 6. Therefore, in the simplest case of RANS (Reynolds Averaged Navier Stokes) turbulence modeling, Navier-Stokes equations along with two equations for turbulent modeling and two equations for transition modeling would result in eight heavily coupled partial differential equations in 3D.

Through discretization, these PDEs are converted into algebraic equations. The number of resulting algebraic equations is equal to the number of computational nodes multiplied by the number of equations (eight in this case). The number of computational nodes depends on the geometry and the size of the domain. For a wind turbine simulation the minimum number of nodes could be in the order of millions. Direct solving of this huge system of equations is not possible and one needs to iterate to get the solution.

Although RANS simulations are far less expensive compared to other types of simulation, still the resulting system of equations is time consuming, making it unsuitable for the design process in which the designer needs to test different configuration to achieve the best design.

Aside from the simulation time, solving the Navier-Stokes equations doesn't satisfy the second criteria established in previous chapter. It was mentioned that a good designing method should have the ability to guide the designer towards the best possible design. In fact Navier-stokes equations are so complex in nature that one cannot acquire enough information from the flow field before they are solved. Therefore, there is a need for simpler models that can, at least, capture and highlight the most dominant features of the flow. A possible method is investigated in the following chapter.

3 Inviscid flow

As described in Chapter 2, Eq.s (2.1.1) and (2.1.2) are so complex that closed form solution, except for very simple geometries doesn't exist. This section addresses the question of how and in what circumstances these equations can be simplified.

3.1 Inviscid flow

The last term in Eq. (2.1.2) describes the action of viscous forces acting on the fluid element. The viscous forces are the product of fluid viscosity and the velocity gradient. For many engineering fluids, the viscosity is very small, meaning that viscous forces could be important only in regions where large velocity gradients exist. In a more exact way, one needs to look at the importance of the viscous forces compared to other terms in Eq. (2.1.2). This can neatly be done by introducing the following non-dimensional variables:

$$\begin{aligned} x^* &= \frac{x}{L} & y^* &= \frac{y}{L} & z^* &= \frac{z}{L} \\ u^* &= \frac{u}{V} & v^* &= \frac{v}{V} & w^* &= \frac{w}{V} \\ t^* &= \frac{t}{T} & p^* &= \frac{p}{P_0} \end{aligned} \tag{3.1.1}$$

where L, V, P_0 are reference length, speed and pressure and T is a characteristic time. If the reference quantities are properly selected, then the non-dimensional variables will be of order 1. Inserting these non-dimensional values into Eq.s (2.1.1) and (2.1.2) one arrives at the following equation for continuity [9]:

$$\frac{\partial u^*}{\partial x^*} + \frac{\partial v^*}{\partial y^*} + \frac{\partial w^*}{\partial z^*} = 0 \tag{3.1.2}$$

and the momentum equation in the x direction:

$$\left(\frac{L}{TV}\right) \frac{\partial u^*}{\partial t^*} + u^* \frac{\partial u^*}{\partial x^*} + v^* \frac{\partial u^*}{\partial y^*} + w^* \frac{\partial u^*}{\partial z^*} = - \left(\frac{P_0}{\rho V^2}\right) \frac{\partial p^*}{\partial x^*} + \left(\frac{\mu}{\rho V L}\right) \left(\frac{\partial^2 u^*}{\partial x^{*2}} + \frac{\partial^2 u^*}{\partial y^{*2}} + \frac{\partial^2 u^*}{\partial z^{*2}}\right) \tag{3.1.3}$$

Outside the boundary layer (in the outer flow region), the non-dimensional variables introduced in Eq. (3.1.1) would be of order 1, meaning that terms having the asterisk in Eq.s (3.1.2) and (3.1.3) would be of order 1 too. Considering the continuity equation, this means that all terms are of the same magnitude and equally important. However, for the momentum equation, the importance of individual terms is determined by the non-dimensional terms appearing before each term. The last group of terms in Eq. (3.1.3), is the viscous term which is multiplied by the inverse of Reynolds number. For the high Reynolds number flows, this term (in the outer flow region) becomes small compared to other terms and can be neglected. Omitting the viscous forces from the Navier-Stokes equations, the solution can be approximated by the Euler equations:

$$\frac{\partial \bar{v}_i}{\partial x_i} = 0 \tag{3.1.4}$$

$$\rho \frac{\partial \bar{v}_i}{\partial t} + \rho \frac{\partial \bar{v}_i \bar{v}_j}{\partial x_j} = - \frac{\partial \bar{p}}{\partial x_i} \tag{3.1.5}$$

These equations are now first order partial differential equations that require one boundary condition for a solid boundary. From physical point of view, lack of viscosity in a flow region means that flow particles near a solid boundary are no longer stopped by the viscous forces and they can freely slip along the boundary. This means that only the normal velocity component on a solid boundary have to be zero.

However, for the region very close to the wall (the boundary layer), the y^* will have the order of magnitude of the boundary layer thickness [7]. This means that the term $\frac{\partial^2 u^*}{\partial y^{*2}}$ in 3.1.3 will be very large and cannot be neglected. The following relation holds for the boundary layer thickness[7]:

$$\delta^* = \frac{\delta}{l} \sim \frac{1}{\sqrt{Re}} \tag{3.1.6}$$

Since y^* is of order $O(\delta^*)$, the continuity equation gives that v^* should also be of order $O(\delta^*)$.

The term $\frac{\partial^2 u^*}{\partial y^{*2}}$ in Eq. (3.1.3) will now be of order $O(\frac{1}{\delta^{*2}})$. The coefficient $\frac{1}{Re}$ is also of order $O(\delta^{*2})$. Thus Navier-stokes equations in two dimension will reduce to the following Prandtl boundary layer equations:

$$\frac{\partial u^*}{\partial x^*} + \frac{\partial v^*}{\partial y^*} = 0 \quad (3.1.7)$$

$$\frac{\partial u^*}{\partial t^*} + u^* \frac{\partial u^*}{\partial x^*} + v^* \frac{\partial u^*}{\partial y^*} = -\frac{\partial p^*}{\partial x^*} + \frac{\partial^2 u^*}{\partial y^{*2}} \quad (3.1.8)$$

$$0 = -\frac{\partial p^*}{\partial y^*} \quad (3.1.9)$$

The last equation implies that the pressure across the boundary layer is constant and the pressure on the solid boundary is equal to the pressure at the boundary layer edge, where the latter can be found by solving the outer inviscid flow equations. Once the inviscid flow equations are solved, one can proceed to solve the boundary layer equations to find the velocity distribution and the shear stress in the boundary layer. The next chapter introduces some concepts and methods for solving the inviscid flow equations.

4 Potential flow

4.1 Irrotational flow

As it was described in the previous chapter, for high Reynolds number flows, the effect of viscosity is limited to the thin boundary layer and the wake. In the outer part of the flow, one can effectively assume an inviscid, incompressible flow. Furthermore, the vorticity equation states that the vorticity created at solid boundary also remains in the boundary layer and the trailing wake [9]. Thus if the incoming flow is irrotational, it remains irrotational in the outer region. The assumption of irrotational flow makes the governing equations even more simpler.

The vorticity is defined as the curl of the velocity vector. The three components of the vorticity vector are defined as:

$$\begin{aligned}\zeta_x &= \left(\frac{\partial w}{\partial y} - \frac{\partial v}{\partial z} \right) \\ \zeta_y &= \left(\frac{\partial u}{\partial z} - \frac{\partial w}{\partial x} \right) \\ \zeta_z &= \left(\frac{\partial v}{\partial x} - \frac{\partial u}{\partial y} \right)\end{aligned}\tag{4.1.1}$$

If the flow is to be irrotational then all the components of the vorticity vector should be zero. This means that:

$$\frac{\partial w}{\partial y} = \frac{\partial v}{\partial z} \qquad \frac{\partial u}{\partial z} = \frac{\partial w}{\partial x} \qquad \frac{\partial v}{\partial x} = \frac{\partial u}{\partial y}\tag{4.1.2}$$

The condition of irrotationality 4.1.2 guaranties the existence of a scalar function ϕ such that:

$$u = \frac{\partial \phi}{\partial x} \qquad v = \frac{\partial \phi}{\partial y} \qquad w = \frac{\partial \phi}{\partial z}\tag{4.1.3}$$

The function ϕ is called a velocity potential. Substitution of Eq. (4.1.3) into continuity equation results in the following equation for the velocity potential:

$$\frac{\partial^2 \phi}{\partial x^2} + \frac{\partial^2 \phi}{\partial y^2} + \frac{\partial^2 \phi}{\partial z^2} = \nabla^2 \phi = 0\tag{4.1.4}$$

The above equation is called Laplace equation which is a linear differential equation. Solving this equation gives the velocity potential and through Eq. (4.1.3) one can get the velocity field. The boundary condition for the Laplace Equation at the solid surfaces is zero normal velocity to the solid boundary. If the velocity field is denoted by \mathbf{q} then:

$$\mathbf{q}_n = 0 \qquad \text{or} \qquad \nabla \Phi \cdot \mathbf{n} = 0\tag{4.1.5}$$

where \mathbf{n} is the normal vector of the solid body. Since the viscosity is neglected, zero tangential velocity cannot be enforced. The solution should also satisfy the boundary condition at infinity. For instance, uniform velocity \mathbf{u} in x direction requires that:

$$\frac{\partial \phi}{\partial x} = \mathbf{u}\tag{4.1.6}$$

There are a number of elementary solutions (e.g.sinks, sources, doublets, vortex) that satisfy the Laplace equation and given boundary conditions. Since the Laplace equation is a linear equation, superposition of elementary solutions is valid and provides another solution satisfying a different set of boundary conditions [9].

Thus, in order to find the flow field around arbitrary bodies, one needs to find the appropriate distribution of elementary solutions satisfying the corresponding boundary conditions.

Nevertheless, it should be noted that, an analytical solution for arbitrary shapes is difficult to find due to complexities of specifying boundary conditions on curved surfaces and also the shape of the wake. In order to find an analytical solution, some approximations of the boundary conditions need to be introduced. One such approximation is the concept of *small disturbance*. A thin airfoil, for example, except for the leading and trailing edge, effectively satisfies the small perturbation approximation. A more detailed treatment of small disturbance approximation is provided in [9].

One important result from the small disturbance solution which will be used in the next section will be mentioned here:

A thin airfoil can be represented by a simple vortex element (lifting element) which is located at the quarter-chord behind the leading edge and the boundary condition of zero normal velocity at the physical surface can be specified at 3/4 chord length behind the leading edge (collocation point).

This representation satisfies the Kutta condition at the trailing edge. The lift force per unit width of this element based on Kutta-Joukowski theory [9] is:

$$L = \rho \Gamma W \quad (4.1.7)$$

where W is the local free stream velocity. The lift coefficient C_l is defined as:

$$C_l = \frac{L}{\frac{1}{2} \rho W^2 c} \quad (4.1.8)$$

where L is the lift force per unit width, ρ is the density of the fluid and c is the chord length of the airfoil. By combining Eq.s (4.1.8) and (4.1.7) the following useful formula can be achieved which relates the circulation of the lumped-vortex element to the C_l value of the airfoil:

$$\Gamma = \frac{C_l W c}{2} \quad (4.1.9)$$

This formula plays an important role in the subsequent section. The C_l value needs to be known to give the circulation. This can either come from experiment or from CFD simulations. In the following section, it is shown how the concept of a lumped-vortex can be used to solve the Laplace equation for 3D flow around a finite wing.

4.2 Finite wing: The lifting line model

In this section Prandtl's lifting line theory is explained for solving the flow field around a 3D finite wing (blade). In this theory each section of the wing is represented as a 2D airfoil section which is modeled by a concentrated vortex element located at the quarter chord length behind the leading edge.

All the local vortices of circulation $\Gamma(y)$ will be placed along a single line, the so-called lifting line. In general, the circulation of the lifting line changes along the blade length. According to Helmholtz's theorem [9], a vortex line cannot start or end in a fluid. Thus any change in the circulation of the vortex line needs to be accompanied by introducing a vortex element in the form of a trailing vortex with the strength equal to the change of circulation of the lifting line. The trailing vortices are shed into the wake and extend infinitely far downstream and become connected again to make a horseshoe vortex. The trailing vortices need to be parallel to the flow so that they don't create any forces. Thus the shape of the wake has to be known or assumed. Figure 4.2.1 demonstrates how a 3D wing is modeled with the lifting line theory.

The straight bound vortex is located 1/4 chord line behind the leading edge. The boundary condition of zero normal velocity is specified 3/4 chord length behind the leading edge (collocation point).

The existence of the trailing vortices brings about lots of complexity to the flow field of a finite wing. It is well known from the vortex theory that vortex lines create a velocity field around them (Biot-Savart law), the so-called induced velocity field. Thus all the trailing vortices in the wake region, create an additional velocity vector at the collocation point. In order to find the velocity vector at the collocation point, the velocity induced by the bound vortex (which is located half a chord length above the collocation point), the velocity induced by

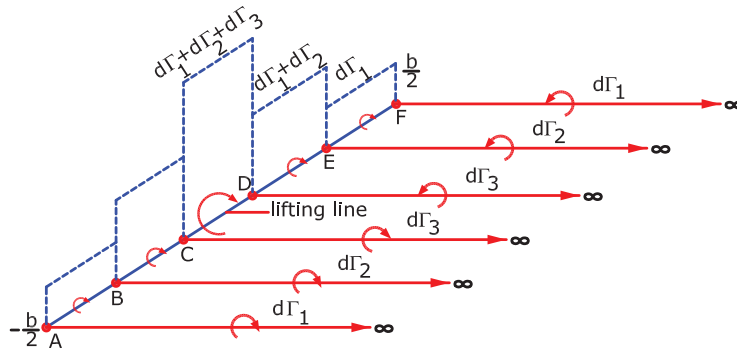


Figure 4.2.1: wing representation in lifting line method, from [2] with permission

all the trailing vortices, and the free stream velocity need to be taken into account. The induced velocity field is dependent on the shape of these vortices. In the simplest case, one can assume that the trailing vortices take the shape of straight lines, parallel to the free stream velocity field.

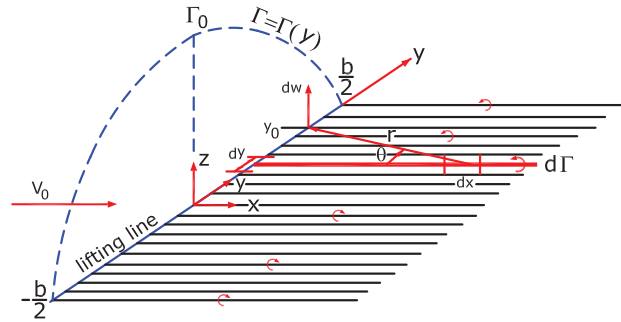


Figure 4.2.2: wing representation in lifting line method, from [2] with permission

Figure 4.2.2 pictures this assumption where the bound vortex (lifting line) is located on the y axis and the trailing vortices, emanating from the bound vortex, parallel to the free stream velocity V_0 which is in the x direction. Figure 4.2.2, however, is not a correct representation of the real physics. Interaction of vortices in the wake region is not taken into account and it is assumed that the vortices in the wake don't change the shape or path of each other. A more realistic picture is shown in figure 4.2.3.

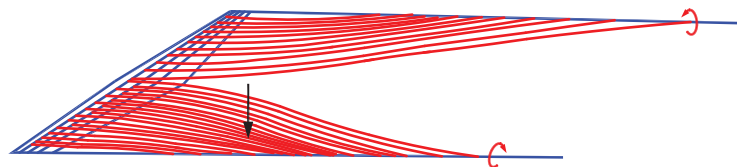


Figure 4.2.3: realistic vortex lines in the wake region, from [2] with permission

4.2.1 Helical vortex theory for wind turbine

As it was stated earlier, the shape of the trailing vortices needs to be known to be able to compute the induced velocities. For wind turbines, there are two main approaches to handle this problem which differ in the way they treat the shape of the wake, namely:

- Free wake modeling
- Helical vortex theory

In the free wake modeling, the shape of the wake is treated as unknown and there is no restriction on it. In this way, the vortex lines in the wake region, are divided into smaller lines with unknown position that induce velocities on each other. Free vortex modeling is computationally more expensive than the helical vortex modeling as there are much higher number of unknowns.

In helical vortex theory, each vortex line in the wake is restricted to take the shape of a helix with constant radius and constant pitch angle. Of these two parameters, the radius is a known value and is equal to the radial position along the blade from which the vortex line is shed. The pitch angle, however, is unknown which needs to be determined. The pitch angle should be selected such that the vortex line is parallel to the local flow velocity at the bound vortex location(which resembles the blade). Thus it is defined as the ratio of the local velocity component in the axial direction over the velocity component in the radial direction. In other words:

$$\tan \phi = \frac{V_0 + W_z}{r\Omega + W_y} \quad (4.2.1)$$

where V_0 is the wind velocity, Ω is rotational speed of the blade in rad/s , and W_z and W_y are induced velocities due to the trailing vortices at the collocation point which need to be determined, see Fig. 4.2.4.

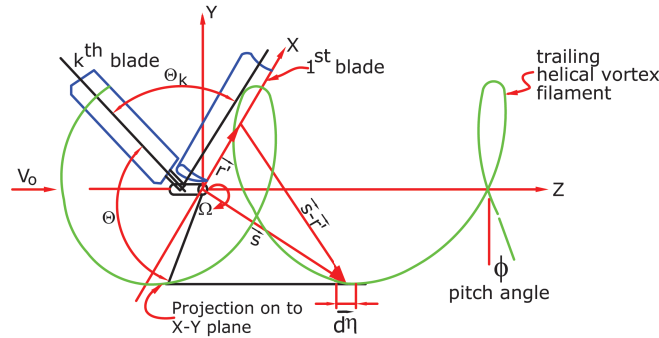


Figure 4.2.4: *helical vortex concept, from [2] with permission*

Once the pitch angles of the helical trailing vortices are known, the induced velocity of individual vortices at any arbitrary positions can be determined. As it is evident from Eq. (4.2.1), since helix pitch angle, which determines the shape of the helix, is a function of induced velocity caused by the wake vortices, the resulting equations become nonlinear and iteration needs to be done to solve for the unknown induced velocity and hence the shape of the helical vortices.

4.2.2 Numerical procedure

Once the shape of the wake is determined, one can proceed to find the induced velocity field of the trailing vortices. First the blade is divided into a number of sections. Each section is represented by a bound line vortex having the length of dr_i with the circulation Γ_i computed from Eq. (4.1.9). The angle of attack is computed based on the local velocity vector. The local velocity vector is the vector summation of free stream velocity and the induced velocity. In general, the circulations of two adjacent segments differ from each other. Thus a trailing vortex should be generated at the boundary of each two successive sections, having a circulation equal to the difference of circulation of the neighbouring segments, making a system of trailing vortices.

The induced velocity field of the trailing vortices is governed by the Biot-Savart law. The induced velocity of a segment, $d\boldsymbol{\eta}$, of a vortex line originated from point \mathbf{r} on the k th blade at the point \mathbf{r}' on the blade based on Biot-Savart law reads as [8]:

$$\mathbf{dw}(r') = \frac{d\Gamma}{4\pi} \frac{(\mathbf{s} - \mathbf{r}') \times d\boldsymbol{\eta}}{|\mathbf{s} - \mathbf{r}'|^3} \quad (4.2.2)$$

where $d\Gamma$ is the circulation of the trailing vortex shed from the blade which is equal to the change in circulation of bound vortex between the points r and $r + dr$ along the blade. The vectors \mathbf{s} , \mathbf{r}' and $d\boldsymbol{\eta}$ are depicted in Fig.4.2.4 and read as:

$$\begin{aligned} \mathbf{r}' &= r'\mathbf{i} \\ \mathbf{s} &= r \cos(\theta + \theta_k) \mathbf{i} + r \sin(\theta + \theta_k) \mathbf{j} + r\theta \tan \phi \mathbf{k} \\ d\boldsymbol{\eta} &= rd\theta \{-\sin(\theta + \theta_k) \mathbf{i} + \cos(\theta + \theta_k) \mathbf{j} + \tan \phi \mathbf{k}\} \end{aligned}$$

where θ is the azimuthal angular variable of the helix measured from the k th blade and ϕ is the pitch angle of the helix determined from Eq. 4.2.1. Eq. 4.2.2 gives the induced velocity of a segment of a vortex line. This equation needs to be integrated with respect to θ to give the induced velocity of a single vortex line at the point \mathbf{r}' . The total induced velocity \mathbf{dw} at the point \mathbf{r}' is the vector summation of induced velocities of all trailing vortices. After performing the cross product operation, integration and summation, it reads as:

$$\mathbf{dw} = dw_x \mathbf{i} + dw_y \mathbf{j} + dw_z \mathbf{k} \quad (4.2.3)$$

where:

$$dw_x = \frac{d\Gamma}{4\pi} \sum_1^N \int_0^\infty \frac{hr [\sin(\theta + \theta_k) - \theta \cos(\theta + \theta_k)]}{A^3} d\theta \quad (4.2.4)$$

$$dw_y = \frac{d\Gamma}{4\pi} \sum_1^N \int_0^\infty \frac{h[r' - r \cos(\theta + \theta_k) - r\theta \sin(\theta + \theta_k)]}{A^3} d\theta \quad (4.2.5)$$

$$dw_z = \frac{d\Gamma}{4\pi} \sum_1^N \int_0^\infty \frac{[r^2 - rr' \cos(\theta + \theta_k)]}{A^3} d\theta \quad (4.2.6)$$

$$A = |\mathbf{s} - \mathbf{r}'| = \left(r^2 - 2rr' \cos(\theta + \theta_k) + r'^2 + h^2\theta^2 \right)^{1/2} \quad (4.2.7)$$

$$h = r \tan \phi \quad (4.2.8)$$

In the above equations, \mathbf{N} is the number of blades and

$$\theta_k = \frac{2\pi(N - k)}{N} \quad (4.2.9)$$

If the diameter of the helix is constant, then dw_x is zero. The above system of equations is nonlinear which can be solved by an iterative method. In order to start the iteration procedure, the induced velocity vector is set to zero and therefore the wake vortices can be initialized. Now these vortices create an induced velocity vector at the collocation point and thus change the angle of attack which in turn changes both the pitch angle of the helix and also the circulation of the bound vortex. Based on this, a new system of vortices is created in the second iteration. This procedure is continued until convergence is achieved.

As described in this chapter, the circulation of the bound vortex in each of the control points along the blade is related to the C_l value of the corresponding airfoil through Eq. (4.1.9). Thus the airfoil characteristics should be known for the lifting line method.

Experimental measurements in wind tunnels have been extensively used to gather such data. Although wind tunnel experiments are the most reliable way to acquire airfoil data, they have their own limitations and downside.

First, most of the published data are for the airfoils which are mainly used for aeronautical applications. Even the measurements in different wind tunnels sometimes differ from each other, especially for the angle of attacks after the stall condition. This might be partly due to the unsteady and 3D nature of the flow at higher

angles which makes the measurement difficult. Although this is of little importance for aerospace applications, where the devices are normally working at angle of attacks lower than stall angle, a wind turbine blade often operates in deep stall and accurate measurement has to be performed. Furthermore, most of the published data are quite old and the data for newly designed airfoils are hard to find in literature.

Second, the experiments are usually limited by the maximum achievable Reynolds number in wind tunnels. The maximum achievable Reynolds number for most wind tunnels is about 9 million. Although the range of Reynolds number for today's wind turbines doesn't exceed this limit, it is expected that by continues growth in the size of wind turbines, the future wind turbines would go beyond this limit. Therefore, the need for a method that can overcome these difficulties has motivated the author to explore the capabilities of computational fluid mechanics.

As it was discussed in chapter 2, there are different levels of CFD simulations, ranging from expensive 3D unsteady DNS or LES simulations to much cheaper steady-state RANS simulations. In this thesis, RANS equations in hypothetical 2D steady-state situations will be discussed and numerically solved. The aim is to investigate the potential of RANS simulations for airfoil calculations and not replicating wind tunnel results in any way. The first requirement of a CFD simulation is the mesh generation process. Indeed, mesh generation plays a crucial role in the accuracy and efficiency of numerical simulation. The following section describes a procedure named Hyperbolic grid generation which has proved to generate meshes with high quality for external flow simulation.

5 Hyperbolic Grid Generation

There exists several methods for grid generation which are divided into two main groups, algebraic and partial differential equation (PDE) generation of grids.

Hyperbolic grid generation falls into the PDE group. The method starts with distribution of grid points on a single boundary and generates subsequent layers of the mesh by propagating into the physical domain. With this method, orthogonality of the grid lines can be enforced. Apart from orthogonality equation, a second equation is also solved to provide the control over the distance between grid lines, cell volume in three dimensional space, or the cell area in two dimension.

In the following, the equations proposed by [17] for two dimensional grid generation with control over grid cell area and mesh orthogonality is presented. The governing equations are:

$$x_\xi x_\eta + y_\xi y_\eta = 0 \quad (5.0.1)$$

$$x_\xi y_\eta - y_\xi x_\eta = V \quad (5.0.2)$$

where x and y are Cartesian coordinates and ξ and η are coordinates in the transformed plane and V is the area of the cell. The partial derivative of x and y with respect to ξ and η are discretized with first order accuracy in the η -direction and second order accuracy in ξ -direction with:

$$\begin{aligned} x_\eta &= \frac{x_{i,j} - x_{i,j-1}}{\Delta\eta} & y_\eta &= \frac{y_{i,j} - y_{i,j-1}}{\Delta\eta} \\ x_\xi &= \frac{x_{i+1,j} - x_{i-1,j}}{2\Delta\xi} & y_\xi &= \frac{y_{i+1,j} - y_{i-1,j}}{2\Delta\xi} \end{aligned} \quad (5.0.3)$$

Eq.s (5.0.1) and (5.0.2) can be linearized around a known state x_0, y_0 resulting in the following vector equation:

$$\mathbf{C}\mathbf{P}_\xi + \mathbf{P}_\eta = \mathbf{S} \quad (5.0.4)$$

where

$$\begin{aligned} \mathbf{P}_\eta &= \begin{bmatrix} x \\ y \end{bmatrix}_\eta & \mathbf{P}_\xi &= \begin{bmatrix} x \\ y \end{bmatrix}_\xi \\ C &= \frac{1}{\gamma} \begin{bmatrix} \alpha & \beta \\ \beta & -\alpha \end{bmatrix} & S &= \frac{V + V_0}{\gamma} \begin{bmatrix} -y^0 \\ x^0 \end{bmatrix}_\xi \\ \alpha &= x_\xi^0 x_\eta^0 - y_\xi^0 y_\eta^0 & \beta &= x_\xi^0 y_\eta^0 + x_\eta^0 y_\xi^0 \\ \gamma &= x_\xi^0 x_\xi^0 + y_\xi^0 y_\xi^0 & V^0 &= x_\xi^0 y_\eta^0 - y_\xi^0 x_\eta^0 \end{aligned}$$

The coefficients are calculated from the previous layer, with the ξ -derivatives computed from Eq. (5.0.3) and η -derivative from Eq. (5.0.1) and (5.0.2) as below:

$$\begin{aligned} x_\eta^0 &= \frac{-y_\xi^0 V^0}{x_\xi^0 x_\xi^0 + y_\xi^0 y_\xi^0} \\ y_\eta^0 &= \frac{x_\xi^0 V^0}{x_\xi^0 x_\xi^0 + y_\xi^0 y_\xi^0} \end{aligned} \quad (5.0.5)$$

An adaptive dissipation term [18] defined as:

$$\text{adaptive dissipation} = \frac{1}{2} \lambda_i^{j-1} (\Delta_i \nabla_i) \mathbf{P}_i^j \quad (5.0.6)$$

is added to Eq. (5.0.4) to make it stable. In Eq. (5.0.6), λ is the eigenvalue of the Jacobian matrix \mathbf{C} which is calculated from the previous layer. The adaptive dissipation term in Eq. (5.0.6) is calculated in the j th level and is implicit. Adding the dissipation term to Eq. (5.0.4) and discretizing using Eq. (5.0.3) the following equation is achieved:

$$-\frac{1}{2} (\mathbf{C} + \lambda_i^{j-1}) \mathbf{P}_{i-1}^j + (\mathbf{I} + \lambda_i^{j-1}) \mathbf{P}_i^j + \frac{1}{2} (\mathbf{C} - \lambda_i^{j-1}) \mathbf{P}_{i+1}^j = \mathbf{P}_i^{j-1} + s \quad (5.0.7)$$

The algorithm described above is coded into a MATLAB program to generate grid lines for different airfoils. The program is able to create both C-mesh and O-mesh. The area function V is user defined. In the program it is computed as the cell length multiplied by a desired cell height. A suitable stretching function for the cell height is implemented to allow for the clustering of grid points near the solid boundaries to resolve the boundary layer.

This method is especially useful for external aerodynamic applications where the shape of the outer boundary of the mesh is not important as long as it is placed in the far field. The following figures show the successful implementation of this method to create two types of grids, namely a C-mesh and an O-mesh, around NACA64-618 and DU40-A17 profiles.

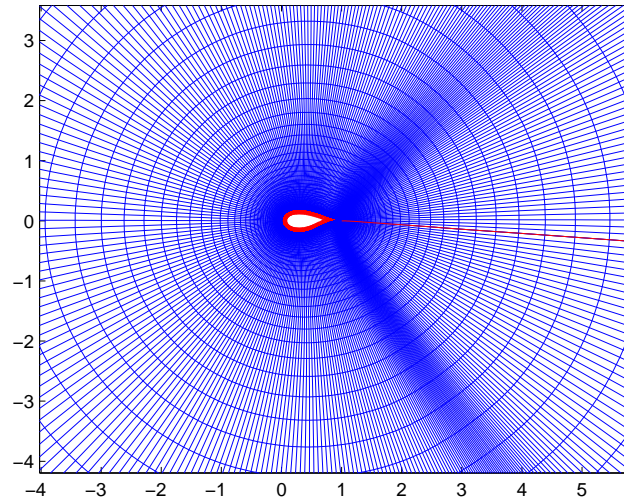


Figure 5.0.1: *O-mesh around DU40*

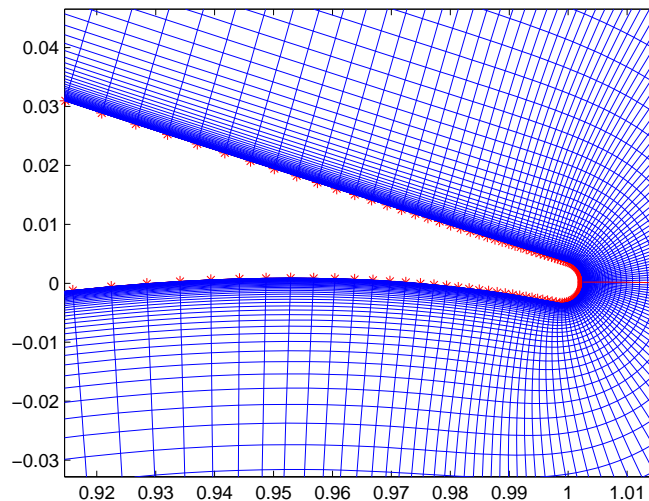


Figure 5.0.2: *O-mesh around DU40, the trailing edge region*

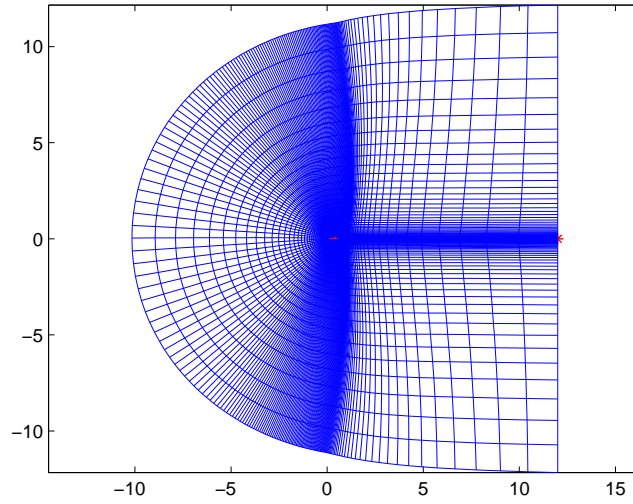


Figure 5.0.3: *C-mesh around NACA 64-618*

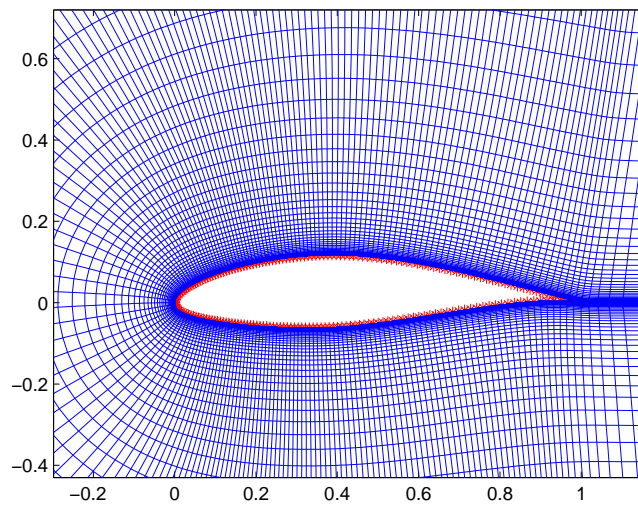


Figure 5.0.4: *C-mesh around NACA 64-618, zoom near the profile*

6 Turbulence Modeling

As discussed in Chapter 2, RANS equations, are the most affordable equations to be solved for many industrial problems. The downside of RANS is the unknown turbulent stresses that appear in the equations. Thus a suitable way of modeling turbulent stresses is needed, leading to the well-known *closure problem*. The best way is to derive exact transport equation for each turbulent stress [5]. This way of handling the closure problem is called Reynolds stress transport model (RSTM) in which a transport equation is derived for each Reynolds stress (six partial differential equations). RSTM equations are derived by taking the second moment of Navier-stokes equations, thus also named second moment closure technique. However, by doing this, more and more unknowns appear in the equations which needs to be modeled. Davidson [3] has used RSTM for calculating the flow field around a high lift airfoil.

The general form of the RSTM equations reads:

$$\frac{\partial \overline{v'_i v'_j}}{\partial t} + \bar{v}_k \frac{\partial \overline{v'_i v'_j}}{\partial x_k} = P_{ij} + \Pi_{ij} + D_{ij} - \varepsilon_{ij} \quad (6.0.1)$$

where the terms on the right hand side are production, pressure-strain, diffusion and dissipation respectively, of which only the production term is exact, whereas the other terms need to be modeled. Nevertheless, having an explicit form for the production term is undoubtedly a major advantage over traditional eddy-viscosity models. The most controversial issue in RSTM is the modeling of pressure-strain term as it plays a crucial role for the evolution and distribution of energy among Reynolds stresses.

RSTM modeling has not gained expected popularity for solving engineering problems due to additional computational time as well as the problems with stability and convergence. In the remainder of this chapter, other methods of addressing the closure problem will be presented.

6.1 Linear Eddy-Viscosity Models

The first researchers in the field of turbulence modeling tried to explain turbulent stresses in a way similar to molecular gradient-diffusion process [22]. In this way, Boussinesq introduce the concept of eddy-viscosity and proposed the following expression relating turbulent stress tensor to the mean strain rate tensor:

$$\overline{v'_i v'_j} = -\nu_t \left(\frac{\partial \bar{v}_i}{\partial x_j} + \frac{\partial \bar{v}_j}{\partial x_i} \right) + \frac{2}{3} \delta_{ij} k \quad (6.1.1)$$

The unknown ν_t is called turbulent viscosity and has the same dimension as ν (kinematic viscosity of the fluid).

Using the eddy viscosity concept, the RANS equations become:

$$\frac{\partial \bar{v}_i}{\partial t} + \frac{\partial \bar{v}_i \bar{v}_j}{\partial x_j} = -\frac{1}{\rho} \frac{\partial \bar{p}}{\partial x_i} + \frac{\partial}{\partial x_j} \left[(\nu + \nu_t) \frac{\partial \bar{v}_i}{\partial x_j} \right] \quad (6.1.2)$$

As it can be seen from Eq. (6.1.2), the effect of turbulent motion appears as an additional viscosity coefficient in the mean flow equations, increasing the diffusion process (which is in agreement with our thought of turbulent flow, being more diffusive than a laminar one). From mathematical point of view, this extra viscosity makes the equations more stable when solved numerically.

Using the Boussinesq assumption, the closure problem reduces to finding an appropriate way of modeling the unknown eddy viscosity. The way in which eddy viscosity is modeled, varies from simple algebraic models to more complex models which involve solving differential equations. From dimensional point of view, viscosity has the dimension of velocity times length. Various models of turbulence propose different approaches for determining the velocity and length scale.

Algebraic models are nowadays considered to be outdated and are seldom used for engineering applications. In these models, the velocity scale is based on some local flow mean velocity or vorticity (Baldwin-Lomax model) and the length scale is related to some typical flow dimensions which requires a prior knowledge of the flow of interest. Prandtl's mixing length theory is an example of algebraic models in which the eddy viscosity is modeled as:

$$\nu_t = \rho l^2 \left| \frac{dU}{dy} \right| \quad (6.1.3)$$

where l is the mixing length.

In "one equation models of turbulence" a transport equation for the velocity scale is solved, whereas the length scale, as in zero equation models, needs to be known a priori. Historically, turbulent kinetic energy, k , is chosen as the basis for the velocity scale and a modeled partial differential equation representing the exact equation for k is solved. This has the advantage of considering the dependence of turbulent stresses on the flow history [22].

The model of Spalart and Allmaras, which is categorized as one equation models, solves a transport equation for the eddy viscosity itself. This model, has gained considerable popularity for aeronautical applications.

Except for the Spalart-Allmaras model, the previous zero and one equation models are incomplete in a sense that a prior knowledge of the flow is required for solving the turbulent field. This shortcoming is lifted at the *two equation* closure models, where a separate transport equation is solved to determine the length scale. Due to this property, two-equation models have gained popularity in every-day engineering applications and simulations. Two-equation models differ from each other in a sense that they solve different equation for the length scale. In what follows, some of most popular two-equation models will be presented and discussed.

6.1.1 The $k - \varepsilon$ model

The transport equation for k can be derived by taking the trace of Eq. (6.0.1) and dividing by two:

$$\frac{\partial k}{\partial t} + \bar{v}_j \frac{\partial k}{\partial x_j} = P_k - \varepsilon + D_t^k + \nu \frac{\partial^2 k}{\partial x_j \partial x_j} \quad (6.1.4)$$

The first term on the right side is the production term which reads as:

$$P_k = -\overline{v_i' v_j'} \frac{\partial \bar{v}_i}{\partial x_j} \quad (6.1.5)$$

This term needs to be modeled due to the presence of the Reynolds stress tensor which is unknown. This term is of significant importance and the success of a turbulence model is highly influenced by how correct this term is modeled. In linear eddy viscosity models this term is modeled by the use of Boussinesq assumption:

$$P_k = -\overline{v_i' v_j'} \frac{\partial \bar{v}_i}{\partial x_j} = \nu_t \left(\frac{\partial \bar{v}_i}{\partial x_j} + \frac{\partial \bar{v}_j}{\partial x_i} \right) \frac{\partial \bar{v}_i}{\partial x_j} = 2\nu_t \bar{S}_{ij} \bar{S}_{ij} \quad (6.1.6)$$

where \bar{S}_{ij} is the symmetric part of the velocity gradient tensor. The velocity gradient tensor is decomposed into a symmetric and anti-symmetric part with the following definitions:

$$\frac{\partial \bar{v}_i}{\partial x_j} = \bar{S}_{ij} + \bar{\Omega}_{ij} \quad (6.1.7)$$

with

$$\bar{S}_{ij} = \frac{1}{2} \left(\frac{\partial \bar{v}_i}{\partial x_j} + \frac{\partial \bar{v}_j}{\partial x_i} \right) \quad \bar{\Omega}_{ij} = \frac{1}{2} \left(\frac{\partial \bar{v}_i}{\partial x_j} - \frac{\partial \bar{v}_j}{\partial x_i} \right) \quad (6.1.8)$$

The second term on the right side of k equation is *dissipation* whose value is determined from its own transport equation. The third term is turbulent diffusion defined as:

$$D_t^k = -\frac{\partial}{\partial x_j} \overline{v_j' \left(\frac{p'}{\rho} + \frac{1}{2} v_i' v_i' \right)} \quad (6.1.9)$$

which includes fluctuating pressure-velocity correlation and triple velocity correlation. Pressure-velocity correlation is usually neglected and the triple velocity correlation is modeled based on the gradient hypothesis leading to:

$$D_t^k = \frac{\partial}{\partial x_j} \left(\frac{\nu_t}{\sigma_k} \frac{\partial k}{\partial x_j} \right) \quad (6.1.10)$$

The last term in the k equation is viscous diffusion which is explicit and doesn't need any modeling. The modeled turbulent diffusion and viscous diffusion make a total diffusion as:

$$D^k = \frac{\partial}{\partial x_j} \left[\left(\nu + \frac{\nu_t}{\sigma_k} \right) \frac{\partial k}{\partial x_j} \right] \quad (6.1.11)$$

The modeled transport equation for dissipation is very similar to k equation but with different constants and appropriate dimensions. In standard $k - \varepsilon$ model the ε equation reads:

$$\frac{\partial \varepsilon}{\partial t} + \bar{v}_j \frac{\partial \varepsilon}{\partial x_j} = \frac{\varepsilon}{k} (c_{\varepsilon 1} P_k - c_{\varepsilon 2} \varepsilon) + \frac{\partial}{\partial x_j} \left[\left(\nu + \frac{\nu_t}{\sigma_\varepsilon} \right) \frac{\partial \varepsilon}{\partial x_j} \right] \quad (6.1.12)$$

where the group ε/k is multiplied to the production and dissipation terms to correct the dimensions of these terms. The model constants in standard $k - \varepsilon$ model are:

$$\sigma_k = 1 \quad \sigma_\varepsilon = 1.3 \quad c_{\varepsilon 1} = 1.44 \quad c_{\varepsilon 2} = 1.92 \quad (6.1.13)$$

The $c_{\varepsilon 1}$ constant is determined from the study of decaying homogeneous turbulence and $c_{\varepsilon 2}$ constant from the *local equilibrium* of turbulence in the log-law region of boundary layer.

The eddy viscosity can now be determined by a suitable combination of k and ε . Based on dimensional analysis the eddy viscosity is defined as:

$$\nu_t = c_\mu \frac{k^2}{\varepsilon} \quad (6.1.14)$$

The constant c_μ takes the value of 0.09 based on equilibrium turbulence in shear flow.

The standard $k - \varepsilon$ model has some well known deficiencies, especially integration up to the wall is very difficult and damping functions are needed to correct the model's behavior near the wall.

6.1.2 The $k - \omega$ model

The parameter ω in this model defined as:

$$\omega = \frac{\varepsilon}{\beta^* k} \quad (6.1.15)$$

is "the rate of dissipation of energy per unit volume and time" [22] or "dissipation per unit kinetic energy" which serves as the inverse of turbulent time scale. Thus $k^{0.5}/\omega$ defines the turbulent length scale. The standard $k - \omega$ model of Wilcox, has the same structure as $k - \varepsilon$ model and reads as:

$$\frac{\partial k}{\partial t} + \bar{v}_j \frac{\partial k}{\partial x_j} = P_k - \beta^* \omega k + \frac{\partial}{\partial x_j} \left[\left(\nu + \frac{\nu_t}{\sigma_k} \right) \frac{\partial k}{\partial x_j} \right] \quad (6.1.16)$$

$$\frac{\partial \omega}{\partial t} + \bar{v}_j \frac{\partial \omega}{\partial x_j} = \frac{\omega}{k} (c_{\omega 1} P_k - c_{\omega 2} k \omega) + \frac{\partial}{\partial x_j} \left[\left(\nu + \frac{\nu_t}{\sigma_\omega} \right) \frac{\partial \omega}{\partial x_j} \right] \quad (6.1.17)$$

where the model constants are:

$$\sigma_k = 2 \quad \sigma_\omega = 2 \quad c_{\omega 1} = \frac{5}{9} \quad c_{\omega 2} = \frac{3}{40} \quad \beta^* = 0.09 \quad (6.1.18)$$

and the turbulent viscosity can be calculated by:

$$\nu_t = \frac{k}{\omega} \quad (6.1.19)$$

The advantage of $k - \omega$ model over $k - \varepsilon$ is that it can be integrated up to the wall. However, the original $k - \omega$ model is sensitive to the free stream value of k and ω .

6.1.3 The $k - \omega$ SST model

One of the models that has recently gained popularity is the $k - \omega$ SST model of Menter[12]. It was mainly developed for flows with adverse pressure gradients and flows with separation. This model is a combination of $k - \varepsilon$ for the outer region and $k - \omega$ for near wall region. Thus makes the best use of good performance of $k - \omega$ near the wall while avoids the sensitivity of $k - \omega$ model to the free stream ω value. This is neatly done by an appropriate blending function that changes the model smoothly from $k - \omega$ model near the wall to $k - \varepsilon$

in the outer region. For a complete description of how to combine these two models see [5]. The $k - \omega$ SST model reads as:

$$\begin{aligned}\frac{\partial k}{\partial t} + \bar{v}_i \frac{\partial k}{\partial x_i} &= \tilde{P}_k - \beta^* k \omega + \frac{\partial}{\partial x_i} \left[(\nu + \sigma_k \nu_t) \frac{\partial k}{\partial x_i} \right] \\ \frac{\partial \omega}{\partial t} + \bar{v}_i \frac{\partial \omega}{\partial x_i} &= \alpha S^2 - \beta \omega^2 + \frac{\partial}{\partial x_i} \left[(\nu + \sigma_\omega \nu_t) \frac{\partial \omega}{\partial x_i} \right] + 2(1 - F_1) \sigma_{\omega 2} \frac{1}{\omega} \frac{\partial k}{\partial x_i} \frac{\partial \omega}{\partial x_i}\end{aligned}\quad (6.1.20)$$

where F_1 function is the blending function controlling the constants appearing in the equations. The constants for near wall region is taken from $k - \omega$ model:

$$\alpha_1 = \frac{5}{9} \quad \beta_1 = \frac{3}{40} \quad \sigma_{k1} = 0.85 \quad \sigma_{\omega 1} = 0.5 \quad (6.1.21)$$

and for the outer region, they are taken from $k - \epsilon$ model:

$$\alpha_2 = 0.44 \quad \beta_2 = 0.0828 \quad \sigma_{k2} = 1 \quad \sigma_{\omega 2} = 0.856 \quad (6.1.22)$$

the $k - \omega$ SST constants are computed by the blending function with the following equation:

$$c = c_1 F_1 + c_2 (1 - F_1) \quad (6.1.23)$$

The blending function F_1 should be chosen such that it takes 1 in the near wall region and 0 in the outer region. This function takes the form of:

$$F_1 = \tanh \left[\left[\min \left(\max \left(\frac{\sqrt{k}}{\beta^* \omega y}, \frac{500\nu}{y^2 \omega} \right), \frac{4\rho \sigma_{\omega 2} k}{CD_{k\omega} y^2} \right) \right]^4 \right] \quad (6.1.24)$$

where:

$$CD_{k\omega} = \max \left(2\rho \sigma_{\omega 2} \frac{1}{\omega} \frac{\partial k}{\partial x_i} \frac{\partial \omega}{\partial x_i}, 10^{-10} \right) \quad (6.1.25)$$

The term $\frac{\sqrt{k}}{\beta^* \omega y}$ is the turbulent length scale divided by y which takes the value of 2.5 in the log-law region and decreases to zero in boundary-layer edge.

The term $\frac{500\nu}{y^2 \omega}$ is the one that control the blending function near the wall. Since in the near wall region ω is of order $O(y^{-2})$, this term assumes a fixed value and makes the blending function take the value 1.

In order to limit the shear stress in adverse pressure gradient flows, Johnson - King model is also incorporated into $k - \omega$ SST model by re-defining the turbulent viscosity as:

$$\nu_t = \frac{a_1 k}{\max(a_1 \omega, F_2 S)} \quad (6.1.26)$$

where S is the norm of strain rate tensor. In adverse pressure gradient flow where the production is large, the term $F_2 S$ becomes large and Eq. (6.1.26) decreases ν_t and thus predicted shear stress decreases. The function F_2 should only be active inside the boundary layer. Thus it is defined with the following terms:

$$F_2 = \tanh \left[\left(\max \left(\frac{2\sqrt{k}}{\beta^* \omega y}, \frac{500\nu}{y^2 \omega} \right) \right)^2 \right] \quad (6.1.27)$$

A production limiter is also added to enhance the behavior of the model in stagnation regions. The new production term in k equation is defined as:

$$\tilde{P}_k = \min(P_k, 10\beta^* \rho k \omega) \quad (6.1.28)$$

where P_k is the original production term of k equation defined in Eq. (6.1.6).

The only difficulty regarding the implementation of this model in comparison with $k - \omega$ or $k - \epsilon$ is the necessity of computing the distance from the wall for computing the blending functions.

6.2 Non-Linear Eddy-Viscosity Models

Linear eddy viscosity models (LEVM) have been in extensive use for turbulent flows calculations. This is partly due to their simplicity and robust implementation in commercial CFD codes, a property that RSTM models fail in some applications.

However, the simplicity contained in their formulations, prevents these models to account for some important features of the complex flow fields. Examining LEVMs reveals that only the strain rate tensor controls the model behavior and no explicit dependence on the rotation tensor exists in these models. The strain rate tensor is frame-independent, meaning that turbulence equations don't differ in inertial and rotating frames. Besides, the linear strain-stress relation in the form of boussinesq assumption results in an isotropic eddy viscosity. Isotropic eddy viscosity is considered to be the main reason of the inability of LEVM for predicting secondary flows in a flow field.

With Boussinesq assumption, Reynolds stress anisotropy tensor defined by:

$$b_{ij} = \tau_{ij} - \frac{2}{3}k\delta_{ij} \quad (6.2.1)$$

$$\tau_{ij} = \overline{v'_i v'_j}$$

can be written as:

$$b_{ij} = -2\nu_t \overline{S}_{ij} \quad (6.2.2)$$

The idea behind nonlinear eddy viscosity models (NLEVM) is to extend Eq. (6.2.2) in a general way to include other nonlinear terms.

6.2.1 Explicit Algebraic Reynolds Stress Model formulation

Explicit Algebraic Reynolds Stress Models (EARSMS) are a class of NLEVM in which the nonlinear terms are derived in a systematic way. In fact, EARSMS lies between LEVM and RSTM. The starting point for EARSMS is the transport equation for the normalized anisotropy tensor:

$$a_{ij} = \frac{b_{ij}}{k} = \frac{\tau_{ij}}{k} - \frac{2}{3}\delta_{ij} \quad (6.2.3)$$

Taking the material derivative results in:

$$\frac{Da_{ij}}{Dt} = \frac{1}{k} \frac{D\tau_{ij}}{Dt} - \frac{\tau_{ij}}{k^2} \frac{Dk}{Dt} \quad (6.2.4)$$

or

$$k \frac{Da_{ij}}{Dt} = \frac{D\tau_{ij}}{Dt} - \frac{\tau_{ij}}{k} \frac{Dk}{Dt} \quad (6.2.5)$$

inserting the terms for τ_{ij} from Eq. (6.0.1) and $\frac{Dk}{Dt}$ from Eq. (6.1.4) into Eq. (6.2.5) and rearranging gives:

$$k \frac{Da_{ij}}{Dt} - \left(D_{ij} - \frac{\tau_{ij}}{k} D^k \right) = P_{ij} + \Pi_{ij} - \varepsilon_{ij} - \frac{\tau_{ij}}{k} (P - \varepsilon) \quad (6.2.6)$$

In order to solve this equation, the following two assumptions are made in EARSMS:

$$\frac{Da_{ij}}{Dt} = 0 \quad (6.2.7)$$

$$D_{ij} = \frac{\tau_{ij}}{k} D^k \quad (6.2.8)$$

The first assumption implies that turbulence has reached the equilibrium state. Using these assumptions, the left side of Eq. (6.2.6) becomes zero and thus the following equation can be achieved:

$$P_{ij} + \Pi_{ij} - \varepsilon_{ij} = \frac{\tau_{ij}}{k} (P - \varepsilon) \quad (6.2.9)$$

This is an implicit equation for a_{ij} . In order to solve this equation, models for ε_{ij} and Π_{ij} are needed. This thesis, follows the procedure and models described in Wallin [21]. In this regard, the dissipation tensor is replaced by isotropic dissipation:

$$\varepsilon_{ij} = \frac{2}{3}\varepsilon\delta_{ij} \quad (6.2.10)$$

The slow pressure strain term is modeled using Rotta model:

$$\Pi_{ij}^s = -c_1\varepsilon a_{ij} \quad (6.2.11)$$

and the rapid pressure by the linear model of Launder, Reece and Rodi:

$$\Pi_{ij}^r = -\frac{c_2 + 8}{11} \left(P_{ij} - \frac{2}{3}P\delta_{ij} \right) - \frac{30c_2 - 2}{55}k \left(\frac{\partial\bar{v}_i}{\partial x_j} + \frac{\partial\bar{v}_j}{\partial x_i} \right) - \frac{8c_2 - 2}{11} \left(\Psi_{ij} - \frac{2}{3}P\delta_{ij} \right) \quad (6.2.12)$$

All of these terms need to be written in terms of a_{ij} and strain rate and vorticity tensors. In order to do so, first the rotation and strain rate tensor are normalized by some appropriate time scale. In case of $k - \varepsilon$ model, k/ε is a relevant choice. Thus:

$$\bar{S}_{ij}^* = \frac{k}{2\varepsilon} \left(\frac{\partial\bar{v}_i}{\partial x_j} + \frac{\partial\bar{v}_j}{\partial x_i} \right) \quad \bar{\Omega}_{ij}^* = \frac{k}{2\varepsilon} \left(\frac{\partial\bar{v}_i}{\partial x_j} - \frac{\partial\bar{v}_j}{\partial x_i} \right) \quad (6.2.13)$$

The production term P_{ij} can be expressed as:

$$\begin{aligned} P_{ij} &= -\overline{v'_i v'_k} \frac{\partial\bar{v}_j}{\partial x_k} - \overline{v'_j v'_k} \frac{\partial\bar{v}_i}{\partial x_k} \\ &= -\left(ka_{ik} + \frac{2}{3}\delta_{ik}k \right) \frac{\varepsilon}{k} (\bar{S}_{jk}^* + \bar{\Omega}_{jk}^*) - \left(ka_{jk} + \frac{2}{3}\delta_{jk}k \right) \frac{\varepsilon}{k} (\bar{S}_{ik}^* + \bar{\Omega}_{ik}^*) \end{aligned}$$

dividing both side by ε :

$$\begin{aligned} \frac{P_{ij}}{\varepsilon} &= -(a_{ik}\bar{S}_{jk}^* + a_{jk}\bar{S}_{ik}^*) - (a_{ik}\bar{\Omega}_{jk}^* + a_{jk}\bar{\Omega}_{ik}^*) - \left(\frac{2}{3}\delta_{ik}\bar{S}_{jk}^* + \frac{2}{3}\delta_{jk}\bar{S}_{ik}^* \right) \\ &= -\frac{4}{3}\bar{S}_{ij}^* - (a_{ik}\bar{S}_{kj}^* + \bar{S}_{ik}^*a_{kj}) + a_{ik}\bar{\Omega}_{kj}^* - a_{kj}\bar{\Omega}_{ik}^* \end{aligned}$$

One can find P/ε by taking the trace of the above equation and division by two, noting that:

$$\begin{aligned} \bar{S}_{ii}^* &= 0 && \text{Continuity} \\ a_{ik}\bar{\Omega}_{ki}^* &= 0 && \text{product of symmetric and antisymmetric matrix} \end{aligned}$$

Thus:

$$\frac{P}{\varepsilon} = a_{ik}\bar{S}_{ki}^*$$

In a similar way the term Ψ_{ij} , defined by:

$$\Psi_{ij} = -\overline{v'_i v'_k} \frac{\partial\bar{v}_k}{\partial x_j} - \overline{v'_j v'_k} \frac{\partial\bar{v}_k}{\partial x_i}$$

can be written as:

$$\begin{aligned} \frac{\Psi_{ij}}{\varepsilon} &= -\left(a_{ik} + \frac{2}{3}\delta_{ik} \right) (\bar{S}_{kj}^* + \bar{\Omega}_{kj}^*) - \left(a_{jk} + \frac{2}{3}\delta_{jk} \right) (\bar{S}_{ki}^* + \bar{\Omega}_{ki}^*) \\ &= -(a_{ik}\bar{S}_{kj}^* + a_{jk}\bar{S}_{ki}^*) - (a_{ik}\bar{\Omega}_{kj}^* + a_{jk}\bar{\Omega}_{ki}^*) - \left(\frac{2}{3}\delta_{ik}\bar{S}_{kj}^* + \frac{2}{3}\delta_{jk}\bar{S}_{ki}^* \right) \\ &= -\frac{4}{3}\bar{S}_{ij}^* - (a_{ik}\bar{S}_{kj}^* + \bar{S}_{ik}^*a_{kj}) - a_{ik}\bar{\Omega}_{kj}^* + a_{kj}\bar{\Omega}_{ik}^* \end{aligned}$$

Substituting the formulas for P_{ij}/ε and P/ε and Ψ_{ij}/ε into Eq. (6.2.12) for rapid pressure term and rearranging gives:

$$\Pi_{ij}^r = \frac{4}{5}\bar{S}_{ij}^* + \frac{9c_2 + 6}{11} \left(a_{ik}\bar{S}_{kj}^* + \bar{S}_{ik}^*a_{kj} - \frac{2}{3}a_{km}\bar{S}_{mk}^*\delta_{ij} \right) + \frac{7c_2 - 10}{11} (a_{ik}\bar{\Omega}_{kj}^* - \bar{\Omega}_{ik}^*a_{kj}) \quad (6.2.14)$$

Substitution of these values into Eq. (6.2.9) results in an implicit equation for a_{ij} [21]:

$$\left(c_1 - 1 + \frac{P}{\varepsilon} \right) \mathbf{a} = -\frac{8}{15}\mathbf{S} + \frac{7c_2 + 1}{11} (\mathbf{a}\boldsymbol{\Omega} - \boldsymbol{\Omega}\mathbf{a}) - \frac{5 - 9c_2}{11} \left(\mathbf{a}\mathbf{S} - \mathbf{S}\mathbf{a} - \frac{2}{3}\text{tr}\{\mathbf{a}\mathbf{S}\}\mathbf{I} \right) \quad (6.2.15)$$

an explicit solution can be derived for the above equation with advanced techniques from linear algebra. Pope [13] was the first to show this and introduce the following integrity basis:

$$\begin{aligned} \mathbf{T}^1 &= \mathbf{S}^* & \mathbf{T}^2 &= \mathbf{S}^*\boldsymbol{\Omega}^* - \boldsymbol{\Omega}^*\mathbf{S}^* \\ \mathbf{T}^3 &= \mathbf{S}^{*2} - \frac{1}{3}\{\mathbf{S}^{*2}\}\mathbf{I} & \mathbf{T}^4 &= \boldsymbol{\Omega}^{*2} - \frac{1}{3}\{\boldsymbol{\Omega}^{*2}\}\mathbf{I} \\ \mathbf{T}^5 &= \boldsymbol{\Omega}^*\mathbf{S}^{*2} - \mathbf{S}^{*2}\boldsymbol{\Omega}^* & \mathbf{T}^6 &= \boldsymbol{\Omega}^{*2}\mathbf{S}^* + \mathbf{S}^*\boldsymbol{\Omega}^{*2} - \frac{2}{3}\{\mathbf{S}^*\boldsymbol{\Omega}^{*2}\}\mathbf{I} \\ \mathbf{T}^7 &= \boldsymbol{\Omega}^*\mathbf{S}^*\boldsymbol{\Omega}^{*2} - \boldsymbol{\Omega}^{*2}\mathbf{S}^*\boldsymbol{\Omega}^* & \mathbf{T}^8 &= \mathbf{S}^*\boldsymbol{\Omega}^*\mathbf{S}^{*2} - \mathbf{S}^{*2}\boldsymbol{\Omega}^*\mathbf{S}^* \\ \mathbf{T}^9 &= \boldsymbol{\Omega}^{*2}\mathbf{S}^{*2} + \mathbf{S}^{*2}\boldsymbol{\Omega}^{*2} - \frac{2}{3}\{\mathbf{S}^{*2}\boldsymbol{\Omega}^{*2}\}\mathbf{I} & \mathbf{T}^{10} &= \boldsymbol{\Omega}^*\mathbf{S}^{*2}\boldsymbol{\Omega}^{*2} - \boldsymbol{\Omega}^{*2}\mathbf{S}^{*2}\boldsymbol{\Omega}^* \end{aligned}$$

The anisotropy tensor can now be expressed in terms of integrity basis above as:

$$\mathbf{a} = \sum_n \beta^n \mathbf{T}^n \quad (6.2.16)$$

where the β^n coefficients are functions of the following five invariants:

$$II_S = \text{tr}\{\mathbf{S}^2\}, \quad II_\Omega = \text{tr}\{\boldsymbol{\Omega}^2\}, \quad III_S = \text{tr}\{\mathbf{S}^3\}, \quad IV = \text{tr}\{\mathbf{S}\boldsymbol{\Omega}^2\}, \quad V = \text{tr}\{\mathbf{S}^2\boldsymbol{\Omega}^2\}$$

It should be noted that Eq. (6.2.15) is a nonlinear equation since the term $P/\varepsilon = -\text{tr}\{\mathbf{a}\mathbf{S}\}$ appears on the left side which is a major obstacle for solving this equation. In the original work of Pope [13] and the work of Taulbee[19] as well as Wallin[21], this term remained implicit during the solution, while in the work of Gatski and Speciale[6] the equilibrium value of P/ε is used. A constant P/ε can only be consistent in equilibrium turbulence and gives wrong behavior for large strain rates. Keeping P/ε implicit during the solution can be advantageous as it gives self-consistent solution for different situations despite the fact that applying EARSMS to non-equilibrium flows violates its main assumption.

For two dimensional flow, Wallin and Johnsson [21] showed that this equation has a closed and fully explicit formulation. In this regard, they assumed the constant c_2 to take the value of 5/9 and thus eliminating the last term in Eq. (6.2.15). In this way, only the coefficients β_1 and β_2 become non-zero, having the following forms:

$$\beta_1 = -\frac{6}{5} \frac{N}{N^2 - 2II_\Omega}, \quad \beta_2 = -\frac{6}{5} \frac{1}{N^2 - 2II_\Omega} \quad (6.2.17)$$

where N is the solution of the following cubic equation:

$$N^3 - c'_1 N^2 - \left(\frac{27}{10} II_S + 2II_\Omega \right) N + 2c'_1 II_\Omega = 0 \quad (6.2.18)$$

which has a positive root as:

$$N = \begin{cases} \frac{c'_1}{3} + (P_1 + \sqrt{P_2})^{\frac{1}{3}} + \text{sign}(P_1 - \sqrt{P_2}) |P_1 - \sqrt{P_2}|^{\frac{1}{3}}, & P_2 \geq 0 \\ \frac{c'_1}{3} + 2(P_1^2 - \sqrt{P_2})^{\frac{1}{6}} \cos\left(\frac{1}{3} \arccos\left(\frac{P_1}{\sqrt{P_1^2 - P_2}}\right)\right), & P_2 < 0 \end{cases}$$

where P_1 and P_2 are the following functions:

$$P_1 = \left(\frac{1}{27}c_1'^2 + \frac{9}{20}\mathbf{II}_S - \frac{2}{3}\mathbf{II}_\Omega \right) c_1' \quad P_2 = P_1^2 - \left(\frac{1}{9}c_1'^2 + \frac{9}{10}\mathbf{II}_S + \frac{2}{3}\mathbf{II}_\Omega \right)^3$$

The unknown N is defined as:

$$N = c_1' + \frac{9}{4} \frac{P}{\varepsilon} \quad (6.2.19)$$

with

$$c_1' = \frac{9}{4}(c_1 - 1) \quad c_1 = 1.8$$

Having found β_i coefficients, Reynolds stress anisotropy tensor a_{ij} can be determined through Eq. (6.2.16) and subsequently all the Reynolds stress tensor components. The Reynolds stress tensor can be written in terms of effective viscosity:

$$\tau_{ij} = \frac{2}{3}k\delta_{ij} - 2\nu_t S_{ij} + k a_{ij}^{ext} \quad (6.2.20)$$

The effective viscosity in 2D reads as:

$$\nu_t = -\frac{1}{2}\beta_1 k \tau \quad (6.2.21)$$

and the extra anisotropy:

$$\mathbf{a}^{ext} = \beta_2 (\mathbf{S}\boldsymbol{\Omega} - \boldsymbol{\Omega}\mathbf{S}) \quad (6.2.22)$$

The main advantage of EARSM methodology is a better approximation of Reynolds stresses, which appear both as a source term in the momentum equations and the production term of turbulent kinetic energy equation. In fact, it is as exact as the RSTM as long as the EARSM assumptions are valid. Nevertheless, even in flow fields where these assumptions are not satisfied, EARSM results have proven to be superior over traditional LEVM without substantial complexity and lacking robustness. EARSM can be coupled to any two equation models without difficulty. In the following, two possible variations are presented.

6.2.2 EARSM-BSL- $k - \omega$

Menter [10], combined the EARSM formulation discussed so far, to the BSL- $k - \omega$ two equation model. The BSL- $k - \omega$ formulation is very similar to the SST formulation with some modification in the model constants and with redefined production term based on EARSM. The model reads as:

$$\begin{aligned} \frac{\partial k}{\partial t} + \bar{v}_i \frac{\partial k}{\partial x_i} &= \tilde{P}_k - \beta^* k \omega + \frac{\partial}{\partial x_i} \left[(\nu + \sigma_k \nu_t) \frac{\partial k}{\partial x_i} \right] \\ \frac{\partial \omega}{\partial t} + \bar{v}_i \frac{\partial \omega}{\partial x_i} &= \frac{\gamma \omega}{k} \tilde{P}_k - \beta \omega^2 + \frac{\partial}{\partial x_i} \left[(\nu + \sigma_\omega \nu_t) \frac{\partial \omega}{\partial x_i} \right] + 2(1 - F_1) \sigma_{\omega 2} \frac{1}{\omega} \frac{\partial k}{\partial x_i} \frac{\partial \omega}{\partial x_i} \end{aligned} \quad (6.2.23)$$

The blending function F_1 has the same form as in the SST model. The model constants are the same as SST except for σ_{k1} which is reduced to 0.5. In this model, γ is defined as:

$$\gamma = \frac{\beta}{\beta^*} - \frac{\sigma_\omega \kappa^2}{\sqrt{\beta^*}} \quad (6.2.24)$$

κ is the von-Karman constant. The production term is now defined by:

$$\tilde{P}_k = \min \left(-\tau_{ij} \frac{\partial \bar{v}_i}{\partial x_j}, 10\beta^* k \omega \right) \quad (6.2.25)$$

In the BSL formulation, the turbulent viscosity is simply defined by:

$$\nu_t = \frac{k}{\omega} \quad (6.2.26)$$

The rationale behind this formulation is that the new better treatment of the production term avoids the needs for *ad hoc* like stress limiter as in the SST model.

6.2.3 EARSM-AKN- $k - \varepsilon$

In this model, the Low Reynolds Number $k - \varepsilon$ model of [1] is used for determining the length and velocity scale. This model reads as:

$$\frac{\partial k}{\partial t} + \bar{v}_j \frac{\partial k}{\partial x_j} = P_k - \varepsilon + \frac{\partial}{\partial x_j} \left[\left(\nu + \frac{\nu_t}{\sigma_k} \right) \frac{\partial k}{\partial x_j} \right] \quad (6.2.27)$$

$$\frac{\partial \varepsilon}{\partial t} + \bar{v}_j \frac{\partial \varepsilon}{\partial x_j} = \frac{\varepsilon}{k} (c_{\varepsilon 1} P_k - c_{\varepsilon 2} f_2 \varepsilon) + \frac{\partial}{\partial x_j} \left[\left(\nu + \frac{\nu_t}{\sigma_\varepsilon} \right) \frac{\partial \varepsilon}{\partial x_j} \right] \quad (6.2.28)$$

where ν_t takes the following form:

$$\nu_t = c_\mu f_\mu \frac{k^2}{\varepsilon} \quad (6.2.29)$$

and the damping functions f_2 and f_μ have the following forms:

$$f_2 = \left[1 - \exp \left(-\frac{y^*}{3.1} \right) \right]^2 \left\{ 1 - 0.3 \exp \left[-\left(\frac{R_t}{6.5} \right)^2 \right] \right\} \quad (6.2.30)$$

$$f_\mu = \left[1 - \exp \left(-\frac{y^*}{14} \right) \right]^2 \left\{ 1 + \frac{5}{R_t^{0.75}} \exp \left[-\left(\frac{R_t}{200} \right)^2 \right] \right\} \quad (6.2.31)$$

where

$$R_t = \frac{k^2}{\nu \varepsilon} \quad y^* = \frac{U_\varepsilon y}{\nu} \quad U_\varepsilon = (\varepsilon \nu)^{0.25} \quad (6.2.32)$$

With the use of EARSM formulation, the production term can be calculated by its definition:

$$P_k = -\tau_{ij} \frac{\partial \bar{v}_i}{\partial x_j} \quad (6.2.33)$$

6.3 Transitional Turbulence Modeling

The models presented in previous sections, all assume a fully turbulent boundary layer and the important effect of laminar-turbulent transition is not taken into account. This is obviously against the real physics where the boundary layer on solid boundaries starts from a laminar one and then through the bifurcation process, the laminar boundary layer loses its stability and becomes turbulent.

Although there exists a large number of publications and theories on the transition process, very few of them have the potential to be applied to general CFD codes. The majority of these methods require non-local operations, which is very difficult to implement in CFD codes. For instance, methods based on linear stability analysis, e^n , require tracking the disturbance growth along each streamline and also some prior knowledge of geometry. One successful application of e^n methods for transition modeling is the XFOIL code which is specifically designed for 2D airfoils. This code uses viscous-inviscid coupling approach with the classical boundary layer formulation.

Many researchers have tried to provide correlation formulas to simulate the transition process. Based on experimental studies, they have provided some formulas to correlate free stream conditions such as the pressure gradient and the turbulent intensity to the transition momentum-thickness Reynolds number. The positive side of these models is that they can easily be calibrated for different transition mechanisms. However these models still require non-local operations for calculating boundary layer momentum-thickness. The following sections describes a newly published model by Menter [11], which has formulated the transition by correlation formulas.

6.3.1 Transitional turbulent $k - \omega$ SST model

Recently one model by Menter et.al [11] proposed to solve laminar-turbulent transition phenomena which can be easily encoded in a CFD code. They have used the concept of vorticity Reynolds number of [20] to provide a link between transition onset momentum-thickness from experimental relations to local boundary

layer quantities. This idea eliminates the need for calculating the boundary layer momentum-thickness. The vorticity Reynolds number is defined as:

$$Re_v = \frac{\rho y^2}{\mu} S \quad (6.3.1)$$

where y is the distance to the nearest wall and S is the absolute value of strain-rate tensor.

In a Blasius boundary layer, the following relation holds between the maximum of the vorticity Reynolds number and momentum-thickness Reynolds number:

$$Re_\theta = \frac{\max(Re_v)}{2.193} \quad (6.3.2)$$

This relation is the main bridge between local variables and the correlation based transition equations. In fact, the function Re_v is an indicator of the growth of instability inside the boundary layer. This is true since as the boundary layer grows, the term $y^2 S$ increases and transition happens once a critical value of Re_v is reached. This has also been proved by experiments.

This model uses two transport equations, one for intermittency which triggers the transition locally and the other for transition onset momentum thickness Reynolds number which captures the non-local influence of the turbulent intensity. The second equation plays a central role as it relates the empirical correlation to the onset criteria in the intermittency equation.

The transport equation for intermittency γ reads as:

$$\frac{\partial \rho \gamma}{\partial t} + \frac{\partial \rho v_j \gamma}{\partial x_j} = P_\gamma - E_\gamma + \frac{\partial}{\partial x_i} \left[(\mu + \mu_t \sigma_f) \frac{\partial \gamma}{\partial x_j} \right] \quad (6.3.3)$$

The transition sources are defined as:

$$P_\gamma = 2F_{length} \rho S (\gamma F_{onset})^{0.5} (1 - \gamma) \quad (6.3.4)$$

and the destruction source:

$$E_\gamma = 0.06 \rho \Omega \gamma F_{turb} (50\gamma - 1) \quad (6.3.5)$$

where the two dimensionless functions F_{length} and F_{onset} control the length of the transition region and the location of the transition onset respectively. The transition onset is determined by the following equations:

$$F_{onset1} = \frac{Re_v}{2.193 Re_{\theta c}} \quad (6.3.6)$$

$$F_{onset2} = \min(\max(F_{onset1}, F_{onset1}^4), 2) \quad (6.3.7)$$

$$F_{onset3} = \max\left(1 - \left(\frac{R_T}{2.5}\right)^3, 0\right) \quad (6.3.8)$$

$$F_{onset} = \max(F_{onset2} - F_{onset3}, 0) \quad (6.3.9)$$

In the above equations R_T is defined as:

$$R_T = \frac{\rho k}{\mu \omega} \quad (6.3.10)$$

where $Re_{\theta c}$ is the critical Reynolds number where the intermittency starts to increase in the boundary layer thickness. Based on empirical studies, the following correlation functions are obtained that relate F_{length} and $Re_{\theta c}$ to transition Reynolds number $\tilde{Re}_{\theta t}$:

$$F_{length} = \begin{cases} 398.189 \cdot 10^{-1} + (-119.270 \cdot 10^{-4}) \tilde{Re}_{\theta t} + (-132.567 \cdot 10^{-6}) \tilde{Re}_{\theta t}^2, & \tilde{Re}_{\theta t} < 400 \\ 263.404 + (-123.939 \cdot 10^{-2}) \tilde{Re}_{\theta t} + (-194.548 \cdot 10^{-5}) \tilde{Re}_{\theta t}^2 + (-101.695 \cdot 10^{-8}) \tilde{Re}_{\theta t}^3, & 400 \leq \tilde{Re}_{\theta t} < 596 \\ 0.5 - (\tilde{Re}_{\theta t} - 596.0) \cdot 3.0 \cdot 10^{-4}, & 596 \leq \tilde{Re}_{\theta t} < 1200 \\ 0.3188, & 1200 \leq \tilde{Re}_{\theta t} \end{cases}$$

$$Re_{\theta c} = \begin{cases} \tilde{Re}_{\theta t} - (-396.035 \cdot 10^{-2} - 120.656 \cdot 10^{-4} \tilde{Re}_{\theta t} + 868.230 \cdot 10^{-6} \tilde{Re}_{\theta t}^2 \\ \quad - 696.506 \cdot 10^{-9} \tilde{Re}_{\theta t}^3 + 174.105 \cdot 10^{-12} \tilde{Re}_{\theta t}^4), & \tilde{Re}_{\theta t} \leq 1870 \\ \tilde{Re}_{\theta t} - (593.11 + (\tilde{Re}_{\theta t} - 187.0) \cdot 0.482), & \tilde{Re}_{\theta t} > 1200 \end{cases}$$

In order to correct the behavior of F_{length} for transition at high Reynolds number flows the following modifications are introduced:

$$F_{length} = F_{length}(1 - F_{sublayer}) + 40 \cdot F_{sublayer} \quad (6.3.11)$$

$$F_{sublayer} = e^{-\left(\frac{R_\omega}{0.4}\right)^2} \quad (6.3.12)$$

$$R_\omega = \frac{\rho y^2 \omega}{500 \mu} \quad (6.3.13)$$

For predicting separation induced transition the following modification is given:

$$\gamma_{sep} = \min(2.0 \max(0, \frac{Re_v}{3.235 Re_{\theta c}} - 1) F_{reattach}, 2) F_{\theta t} \quad (6.3.14)$$

$$F_{reattach} = e^{-\left(\frac{R_T}{20}\right)^4} \quad (6.3.15)$$

The effective value of γ is thus obtained by the following:

$$\gamma_{effective} = \max(\gamma, \gamma_{sep}) \quad (6.3.16)$$

The other equation of this model is a transport equation for transition momentum Reynolds number $\tilde{Re}_{\theta t}$ which reads as:

$$\frac{\partial \rho \tilde{Re}_{\theta t}}{\partial t} + \frac{\partial \rho v_j \tilde{Re}_{\theta t}}{\partial x_j} = P_{\theta t} + \frac{\partial}{\partial x_i} \left[2.0(\mu + \mu_t) \frac{\partial \tilde{Re}_{\theta t}}{\partial x_j} \right] \quad (6.3.17)$$

This is a simple convection-diffusion equation with only one source term. The source term is intended to force $\tilde{Re}_{\theta t}$ match the value of $Re_{\theta t}$ outside the boundary layer and is turned off inside the boundary layer, letting $\tilde{Re}_{\theta t}$ simply be diffused in to the boundary layer from the free stream. The source term $P_{\theta t}$ is defined by the local difference of $\tilde{Re}_{\theta t}$ and $Re_{\theta t}$ and a blending function by the following:

$$P_{\theta t} = 0.03 \frac{\rho}{t} (Re_{\theta t} - \tilde{Re}_{\theta t})(1.0 - F_{\theta t}) \quad (6.3.18)$$

where t is a time scale defined by:

$$t = \frac{500 \mu}{\rho U^2} \quad (6.3.19)$$

The blending function $F_{\theta t}$ reads as:

$$F_{\theta t} = \min(\max(F_{wake} \cdot e^{-\left(\frac{y}{\delta}\right)^4}, 1.0 - \left(\frac{\gamma - 1/50}{1.0 - 1/50}\right)^2), 1.0) \quad (6.3.20)$$

with the following parameters:

$$\delta = \frac{50 \Omega y}{U} \cdot \delta_{BL} \quad \delta_{BL} = \frac{15}{2} \theta_{BL} \quad \theta_{BL} = \frac{\tilde{Re}_{\theta t} \mu}{\rho U} \quad (6.3.21)$$

$$F_{wake} = e^{-\left(\frac{Re_\omega}{1E+5}\right)^2} \quad Re_\omega = \frac{\rho \omega y^2}{\mu} \quad (6.3.22)$$

The function F_{wake} is added to make sure that the blending function is not active in the wake region.

The empirical correlation used in this model is based on the pressure gradient parameter and turbulent intensity defined as:

$$\lambda_\theta = \frac{\rho\theta^2}{\mu} \frac{dU}{ds} \quad (6.3.23)$$

$$Tu = 100 \frac{\sqrt{2k/3}}{U} \quad (6.3.24)$$

with Re_θ defined as:

$$Re_{\theta t} = \frac{\rho\theta_t U_0}{\mu} \quad (6.3.25)$$

the following correlation equations are defined:

$$Re_{\theta t} = \left(1173.51 - 589.428Tu + \frac{0.2196}{Tu^2} \right) F(\lambda_\theta) \quad Tu \leq 1.3 \quad (6.3.26)$$

$$Re_{\theta t} = 331.50(Tu - 0.5658)^{-0.671} F(\lambda_\theta) \quad Tu > 1.3 \quad (6.3.27)$$

$$F(\lambda_\theta) = 1 - (-12.986\lambda_\theta - 123.66\lambda_\theta^2 - 405.689\lambda_\theta^3) e^{-\left(\frac{Tu}{1.5}\right)^{1.5}} \quad \lambda_\theta \leq 0 \quad (6.3.28)$$

$$F(\lambda_\theta) = 1 + 0.275(1 - e^{-35.0\lambda_\theta}) e^{-\frac{Tu}{0.5}} \quad \lambda_\theta > 0 \quad (6.3.29)$$

For numerical robustness the following relations are imposed:

$$-0.1 \leq \lambda_\theta \leq 0.1 \quad Tu \geq 0.027 \quad Re_{\theta t} \geq 20 \quad (6.3.30)$$

The empirical correlation equations need to be solved iteratively since the momentum-thickness θ_t appears on both side of the equations. The final output of this transition model is the γ_{eff} defined in Eq. (6.3.16) which controls the production and destruction term of k equation in the original $k - \omega SST$ model in Eq. (6.1.4) through the following equations:

$$\tilde{P}_k = \gamma_{eff} P_k \quad \tilde{D}_k = \min(\max(\gamma_{eff}, 0.1), 1.0) D_k \quad (6.3.31)$$

some modifications is also made to the blending function F_1 as bellow:

$$F_1 = \max(F_{1original}, F_3) \quad F_3 = e^{-\left(\frac{R_y}{120}\right)^8} \quad R_y = \frac{\rho y \sqrt{k}}{\mu} \quad (6.3.32)$$

Node	Radial Position (m)	Twist (deg)	Airfoil Type	Chord (m)
0	9.75	13.31	Circle	3.6
1	11.75	13.31	DU40	4.56
2	15.85	11.48	DU35	4.65
3	19.95	10.16	DU35	4.46
4	24.05	9.01	DU30	4.25
5	28.15	7.79	DU25	4.01
6	32.25	6.54	DU25	3.75
7	36.35	5.36	DU21	3.50
8	40.45	4.18	DU21	3.26
9	44.55	3.12	NACA64	3.01
10	48.65	2.32	NACA64	2.76
11	52.75	1.52	NACA64	2.52
12	56.16	0.86	NACA64	2.31
13	58.90	0.37	NACA64	2.09
14	61.63	0.11	NACA64	1.42
15	63.00	0.0	NACA64	1.00

Table 7.1.1: "NREL Offshore 5 – MW HAWT" Blade geometry

7 Results and discussions

7.1 Lifting line method

The lifting line algorithm presented in Chapter 4 is encoded in a MATLAB Graphical User Interface (GUI). The schematic of the GUI is shown in the following Figure. NREL Offshore 5 MW wind turbine is used as a test case for testing the program. The geometry of the blade is shown in Table 7.1.1. Note that the node number 0 and 15 represent the base and the tip of the blade respectively. These two points will be assigned zero circulation as there is no lift in these positions.

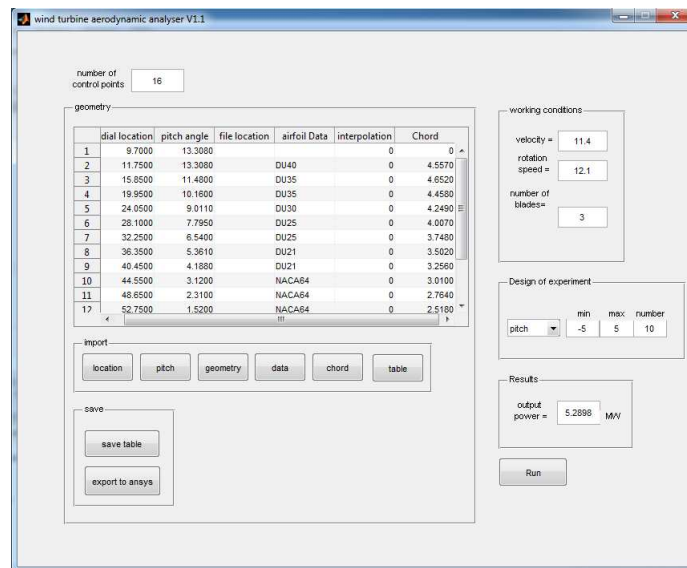


Figure 7.1.1: *wind turbine aerodynamic analyzer V1.1*

The results of applying the lifting line model to "NREL Offshore 5 MW" wind turbine are shown in the following figures. It is clear from these figures how the angle of attack and lift coefficient are decreased due to

the presence of the trailing vortices. The total output power based on this method is about 5.2 MW which indicates an error of approximately 5 percent which is acceptable.

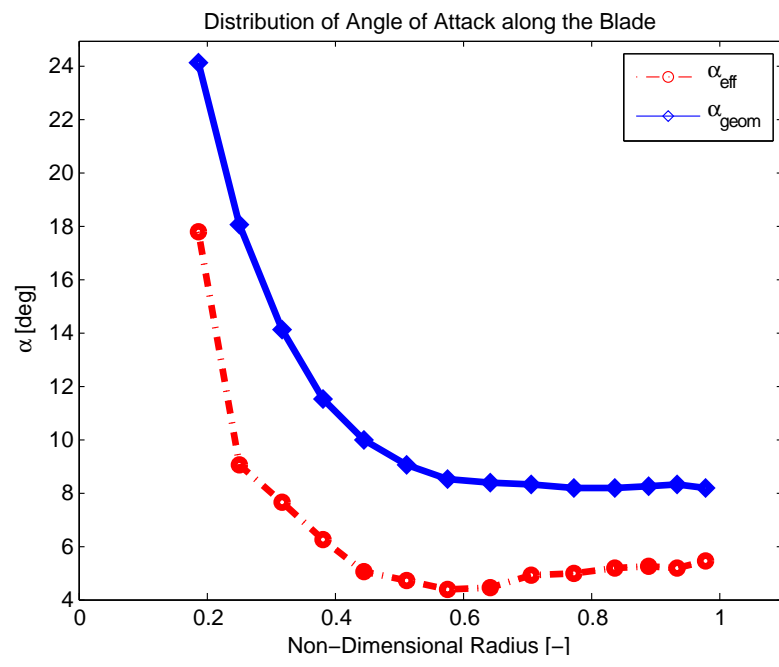


Figure 7.1.2: angle of attack along the blade

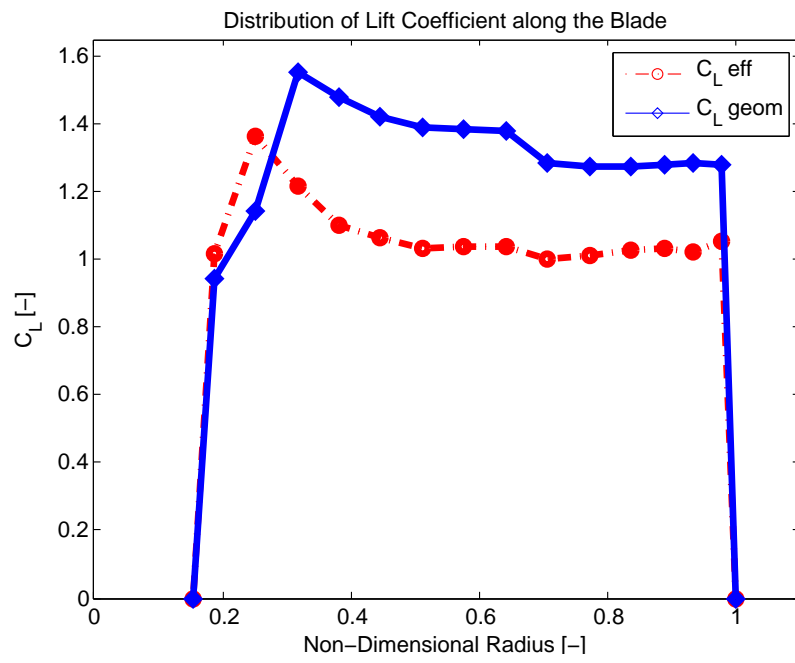


Figure 7.1.3: Lift coefficient

7.2 Flat plate test cases

The transitional turbulence formulations discussed so far are implemented in CALC-BFC code. CALC-BFC is a finite volume code written in FORTRAN 77 language. SIMPELC algorithm is used for pressure-velocity coupling. Moreover, collocated grid arrangement with Rhie-Chow algorithm is implemented in the code. For further information about the code see [4]. In order to validate the model and the implementation in the code, some test cases are simulated and the results are compared with experiments.

The flat-plate test cases used are those of European Research Community on Flow Turbulence and Combustion (ERCOFTAC) T3 series of flat-plate experiments [14, 15]. These test cases all have zero pressure gradient but with different free stream turbulent intensity (FSTI). Besides these test cases, another test case of Schubaur and Klebanof [16], which has a low free stream turbulent intensity but higher inlet velocity, is also simulated. The inlet conditions for these cases at 0.04 m upstream of the leading edge of the plate is summarized in table 7.2.1. A schematic of the computational domain for the simulation is shown in Fig.7.2.1. The inlet is

Table 7.2.1: Inlet conditions for flat-plate test cases

Case	U inlet [m/s]	FSTI	$\frac{\mu_t}{\mu}$	ρ	μ
T3A	5.4	3.3	12.0	1.2	1.8 e-5
T3A-	19.4	0.874	8.72	1.2	1.8e-5
S and K	50.1	0.3	1.0	1.2	1.8e-5

located 0.04 m upstream the leading edge of the plate. The boundary condition at the outlet is set to Neuman boundary condition which corresponds to fully developed flow condition. This is not a realistic boundary condition for this setup since the boundary layer continuously grows and there will be no fully developed flow. This *approximated* boundary condition is justified by the fact that the approximated information at this boundary can only be transported upstream by *diffusion* terms which are very weak compared to convective forces and hence affect the solution of a small number of upstream cells. For the top boundary a Neuman

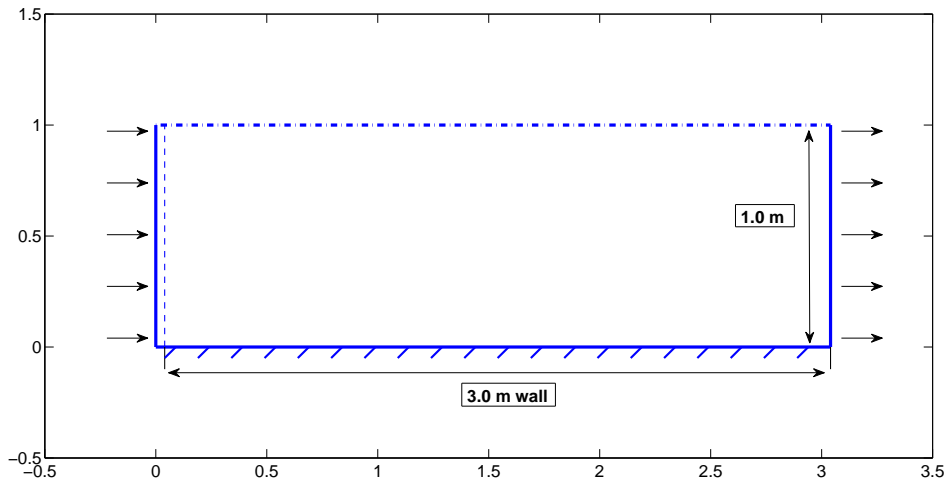


Figure 7.2.1: *computational domain for flat plate simulation*

boundary condition with zero normal flux is specified. This condition is also an approximation of the reality. As the boundary layer develops on the plate, the fluid particles in this region have lack of momentum compared to fluid particles in the free stream. Since all cross sections normal to the plate are equal thus the continuity equation requires that free stream particles gain higher velocities compared to inlet conditions. In reality, however, this doesn't happen and streamlines go out of the box to make a larger cross section and thus there is outflow at the top boundary. Since the boundary layer is very thin, this error can be minimized by locating the top boundary at a large distance to the plate.

7.2.1 $\gamma - \tilde{Re}_\theta$ model

The computational mesh (every second line) is shown in Fig.7.2.2. Grid clustering is employed both at the wall region and the leading edge of the plate and also in the turbulent region. For the expected region of transition, Constant grid spacing is used. The results of simulating these test cases are shown in Figs 7.2.3-7.2.5, where

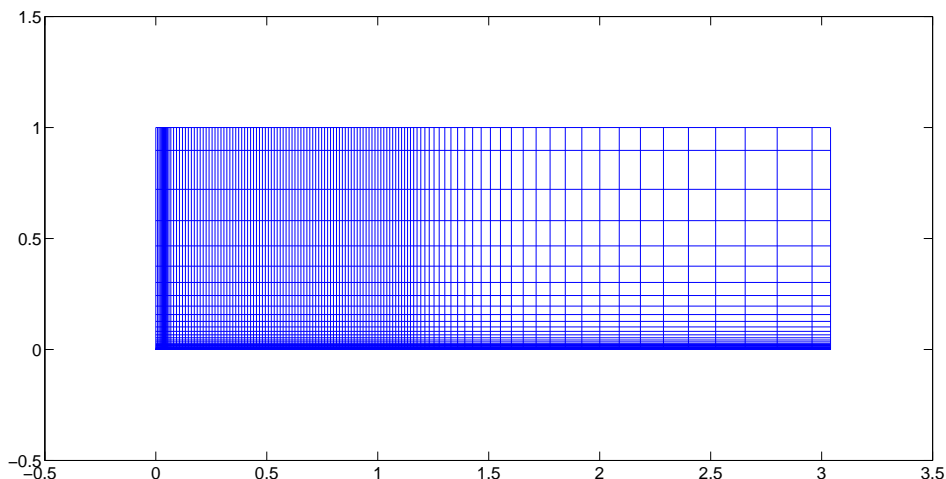


Figure 7.2.2: *computational mesh for T3A flat plate simulation (every second line)*

the skin friction coefficient defined by:

$$C_f = \frac{\tau_{wall}}{0.5\rho U_\infty} \quad (7.2.1)$$

is plotted against the local Reynolds number. For a laminar boundary layer the analytical formula of skin friction coefficient based on Blasius boundary layer solution is used which reads as:

$$C_f = \frac{0.664}{\sqrt{Re_x}} \quad (7.2.2)$$

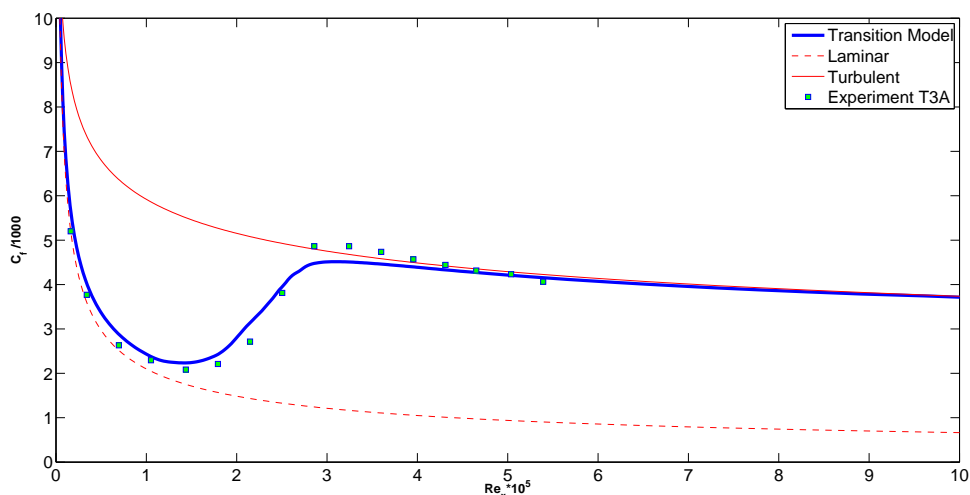


Figure 7.2.3: *T3A test case, comparison of $\gamma - \tilde{Re}_\theta$ transition model with y^+ of 0.2 and experiment*

As it is evident from the figures, the transition predicted with the $\gamma - \tilde{Re}_\theta$ model agrees well with the experiments. This also shows that the transition model is implemented correctly in the **CALC-BFC** code.

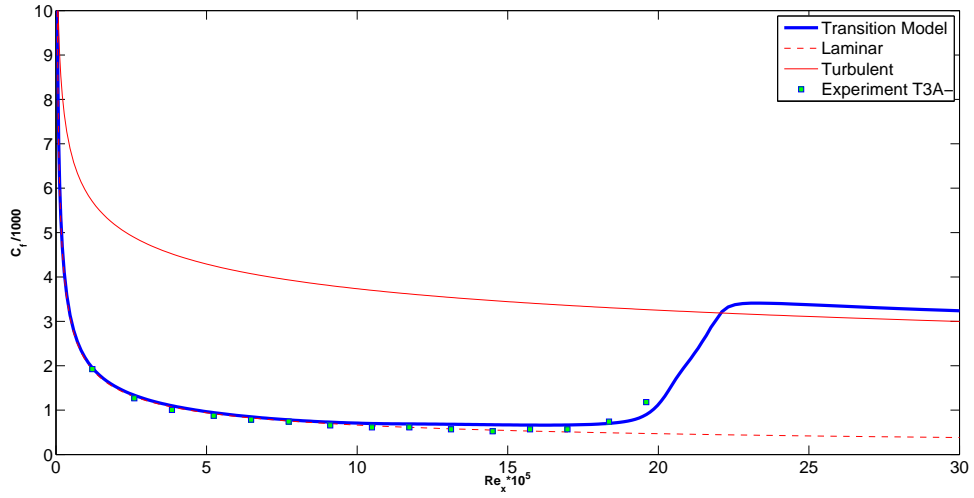


Figure 7.2.4: *T3A-* test case, comparison of $\gamma - \tilde{Re}_\theta$ transition model with y^+ of 0.65 and experiment

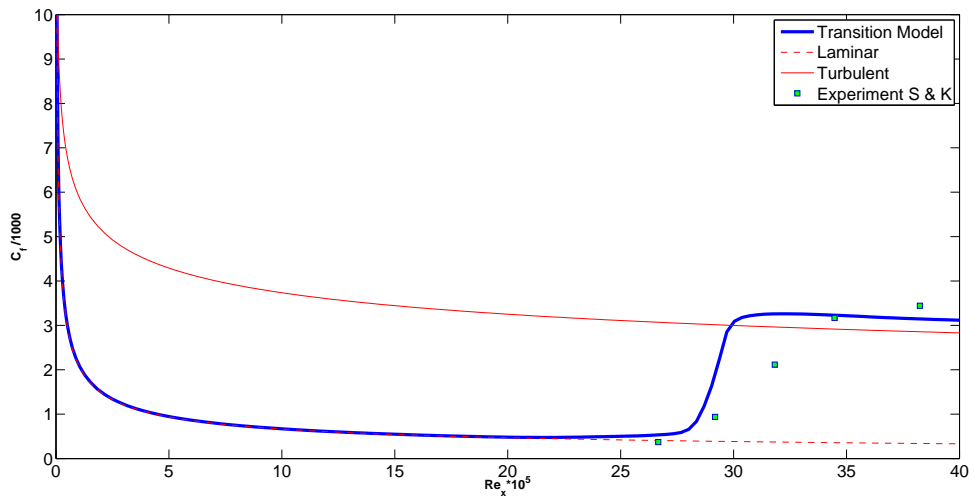


Figure 7.2.5: *S and K* test case, comparison of $\gamma - \tilde{Re}_\theta$ transition model with y^+ of 0.75 and experiment

This model, however is sensitive to the discretization schemes and the y^+ of the first node off the wall. Figure 7.2.6 shows how the predicted point of transition is changed by changing the y^+ for the T3A experiment. The two meshes used, have exactly the same number of grid points and same grid distribution in streamwise direction but with different grid distribution in wall normal direction. The **VanLeer** scheme, which is a

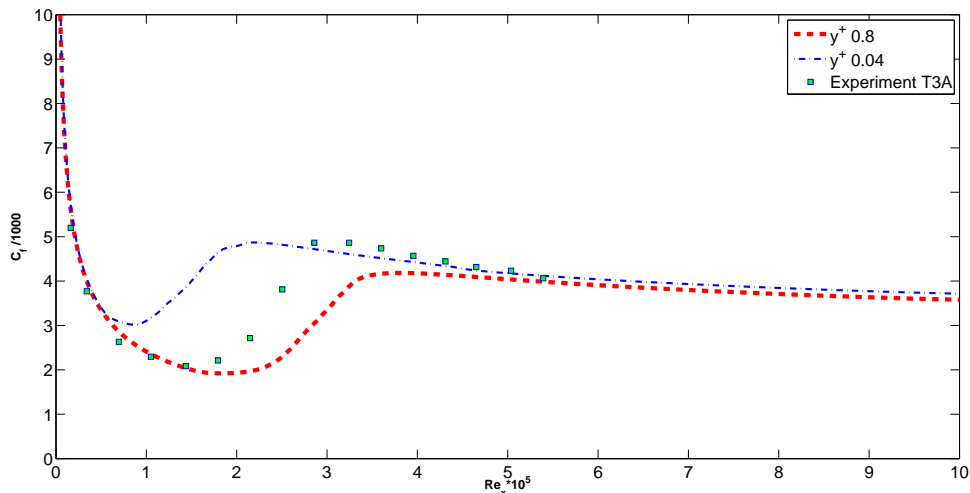


Figure 7.2.6: *T3A experiment, sensitivity of $\gamma - \tilde{Re}_\theta$ transition model to y^+ value of the first node*

second order bounded scheme, is used for momentum equations. A second order **MUSCL** method is used for turbulence and transition equations. The y^+ of the first node is within the range of 0.5 and 0.7.

7.2.2 EARSM model

Fig. 7.2.7 shows the result of simulating T3A test case with EARSM formulation described earlier, where the skin friction coefficient is plotted against Reynolds number along the plate. The extra source term of EARSM formulation (Eq. 6.2.22) is treated explicitly without any difficulty for convergence. This figure shows that in the turbulent region, EARSM-BSL and EARSM-AKN models give different wall shear stress, highlighting the necessity of tuning the original BSL or AKN model coefficients to be used for the EARSM model. Although non of these two formulations are intended for transition, it is clear that the low Reynolds number AKN model has more capability for considering the laminar boundary layer than the BSL model.

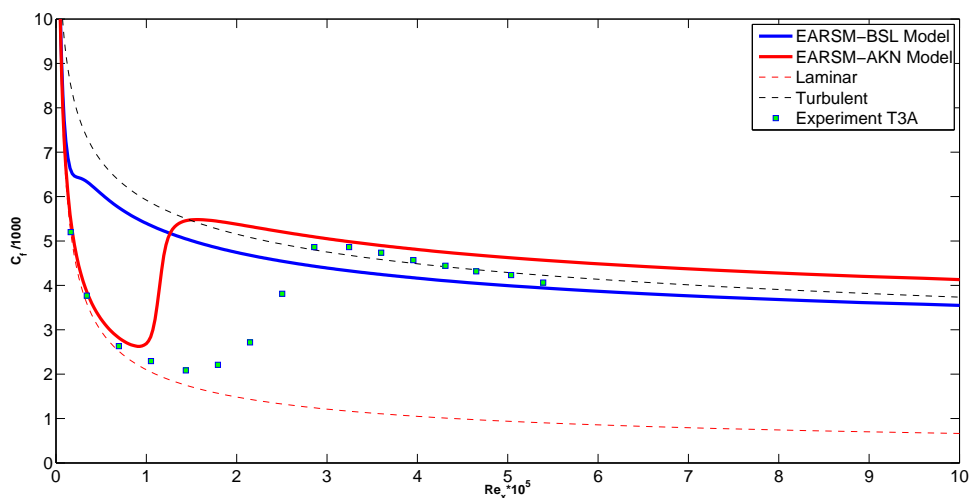


Figure 7.2.7: *T3A test case, comparison EARSM-BSL and EARSM-AKN models and experiment*

7.3 XFOIL program

XFOIL is an interactive program for analysis and design of airfoils which is written by Drela and Youngren in MIT. It combines the speed and accuracy of high order panel methods and a fully coupled viscous-inviscid interaction method. Transition modeling is calculated based on stability e^n method. The source code is written in FORTRAN 77. The trailing edge can either be of sharp or blunt shape. Panel method equations are closed with explicit Kutta condition. In this code, compressibility is taken into account by Karman-Tsien compressibility correction.

A Graphical User Interface in MATLAB is written to enhance working with XFOIL. The schematic of the GUI is shown in the following figure.

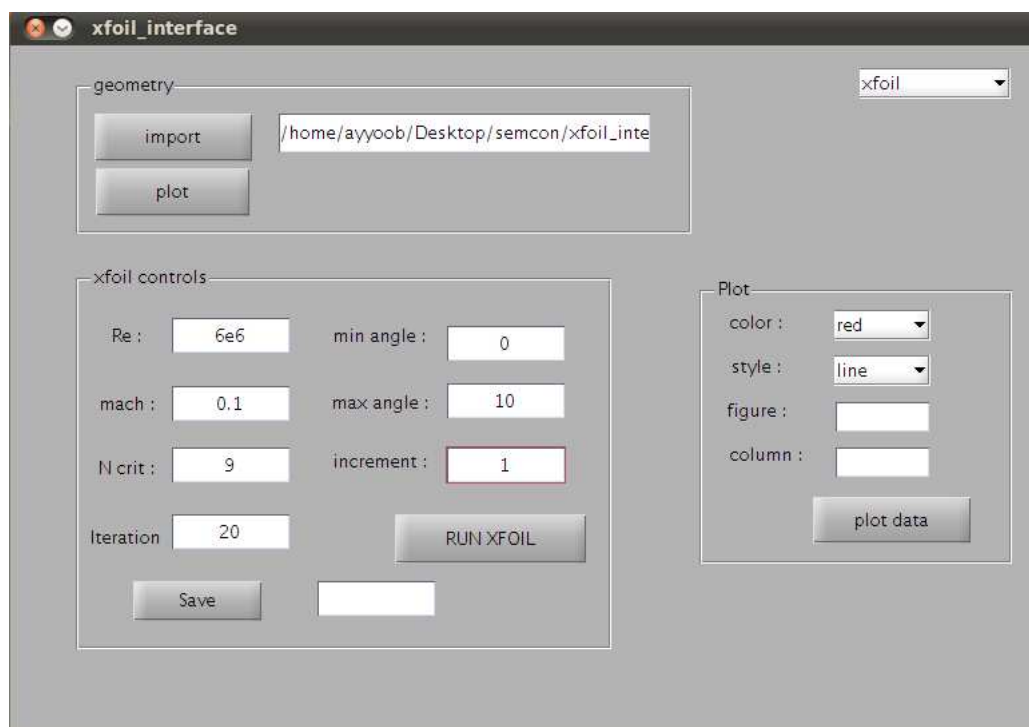


Figure 7.3.1: XFOIL graphical user interface

7.4 Airfoils 2D simulations

In this section, the above turbulent model is applied to different airfoils to get the desired C_l and C_d data to be used for the lifting line method. The meshes used here are all generated with the Hyperbolic mesh generator described earlier. Free stream turbulent intensity is set to 0.07 percent which is equivalent to setting $n=9$ in XFOIL program. The farfield boundary is located at approximately 12 chord length. For DU21 and DU30 airfoils, a 330×100 O-mesh similar to Fig.5.0.1 and 5.0.2 is used, whereas for NACA64_618 profile a 300×100 C-mesh type as shown in fig 5.0.3 and 5.0.4 is employed.

7.4.1 $\gamma - \tilde{Re}_\theta$ model

The results of simulating three cases with the transition model are plotted in the following figures.

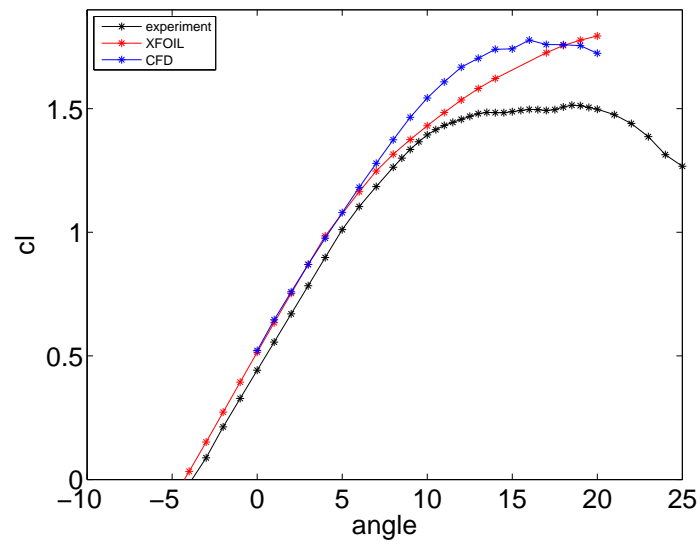


Figure 7.4.1: *NACA64* profile, comparison of different methods for airfoil data

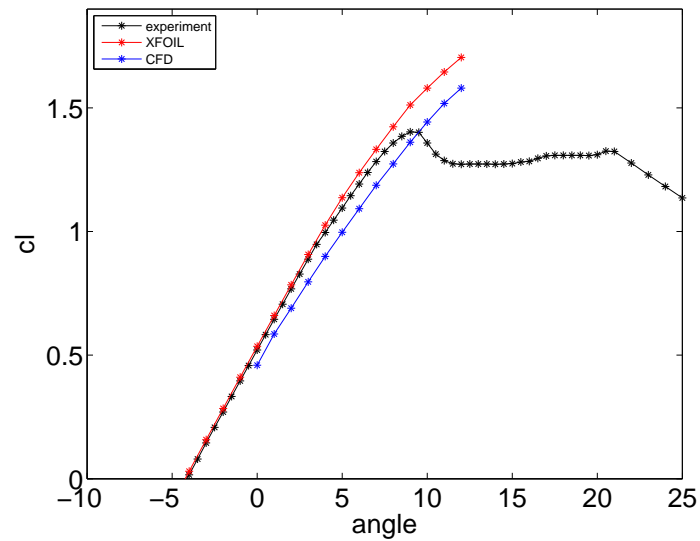


Figure 7.4.2: *DU21* profile, comparison of different methods for airfoil data

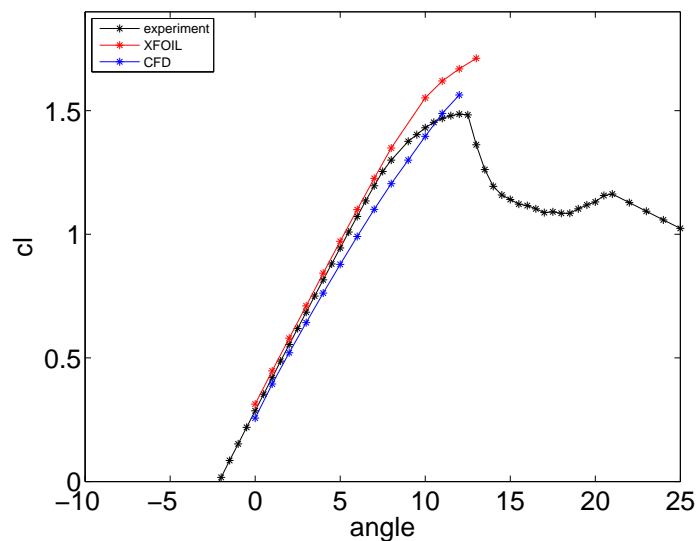


Figure 7.4.3: *DU30 profile, comparison of different methods for airfoil data*

As it is evident from these plots, both XFOIL program and $\gamma - \tilde{R}e_\theta$ CFD model produce approximately similar results for low angle of attacks which is near the experimental measurements. However for higher angle of attacks, both codes have failed to reproduce experimental results. This was expected for the XFOIL code since it is designed for thin airfoils and lower angle of attacks. However for the CFD simulation, this situation might be caused by different reasons. One study in Riso national laboratory in Denmark explained this situation due to the 3D flow features after the stall condition which cannot be captured by 2D steady-state simulations. Though this explanation seems reasonable, the effect of turbulent model should not be under-estimated.

7.4.2 EARSM model

An airfoils simulation with EARSM formulation is a challenging task as the treatment of the extra source term in the momentum equations needs careful consideration. The challenge comes from the fact that, unlike turbulence quantities which have always positive values, the velocity components, in general, can take both positive and negative values. Thus all the source terms, regardless of their sign, should be treated explicitly. This causes instability if there are negative source terms in an equation. A number of numerical tricks are tested in this thesis, but none of them gave acceptable results for the airfoil calculations. Thus this section is left as a future work.

7.5 3D steady-state CFD simulation

In order to evaluate the accuracy of the lifting line method, a 3D steady-state CFD simulation of the problem is done in ANSYS CFX5. The computational domain is shown in the following figure. The domain starts from approximately one blade radius upstream and extends to 3 blade radius downstream. Due to the symmetry of the problem, only one blade is simulated.

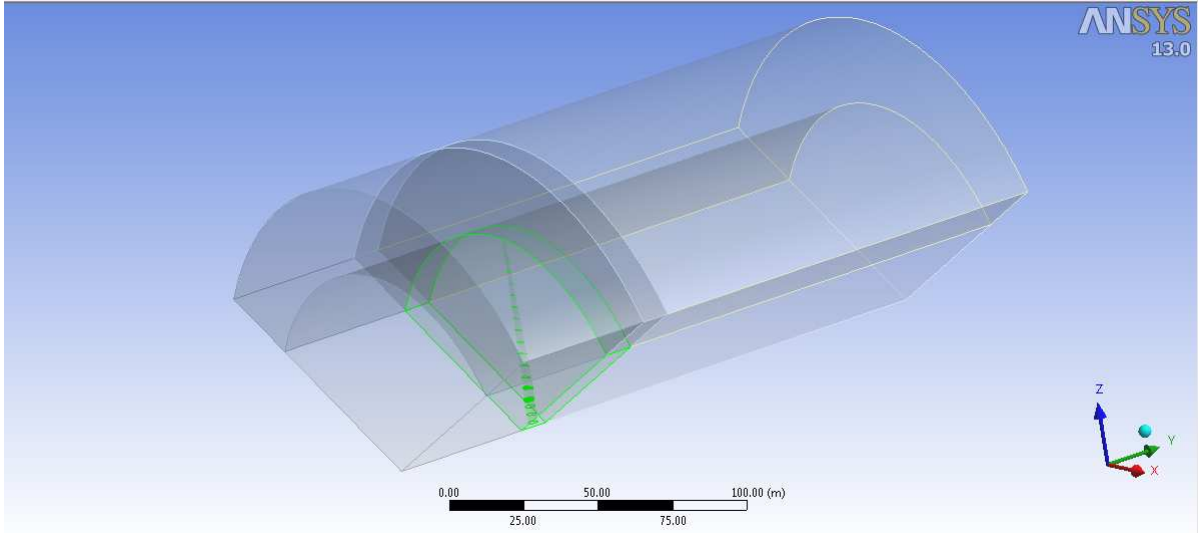


Figure 7.5.1: *Computational domain for the CFD simulation*

The computational mesh is shown in Fig.7.5.2. The cells near the blade are **inflated** to resolve the boundary layer. Here the focus is to maintain the first layer yplus below 2 as is recommended by CFX.

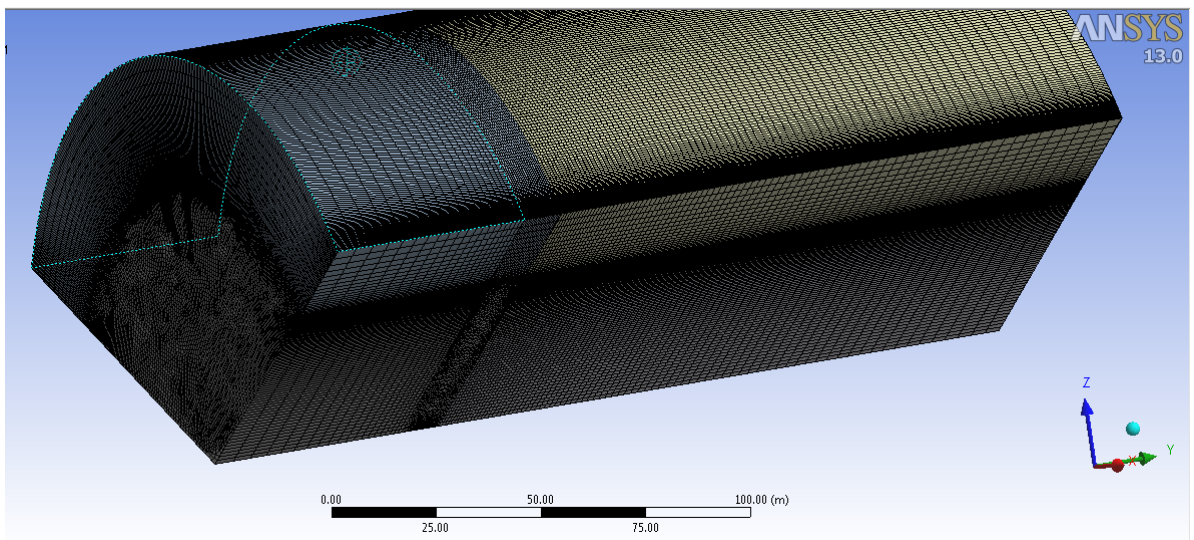


Figure 7.5.2: *Computational mesh for the CFD simulation*

The boundary conditions for the domain are shown in the following figure. Periodic boundary conditions are specified at the left and right boundary. The upper boundary is placed far from the blade so that **open** boundary condition can be specified. Inlet velocity is set to **11.4 m/s**. The other end of the domain has **outlet** boundary condition. The $k - \omega$ SST model is used for Turbulence modeling.

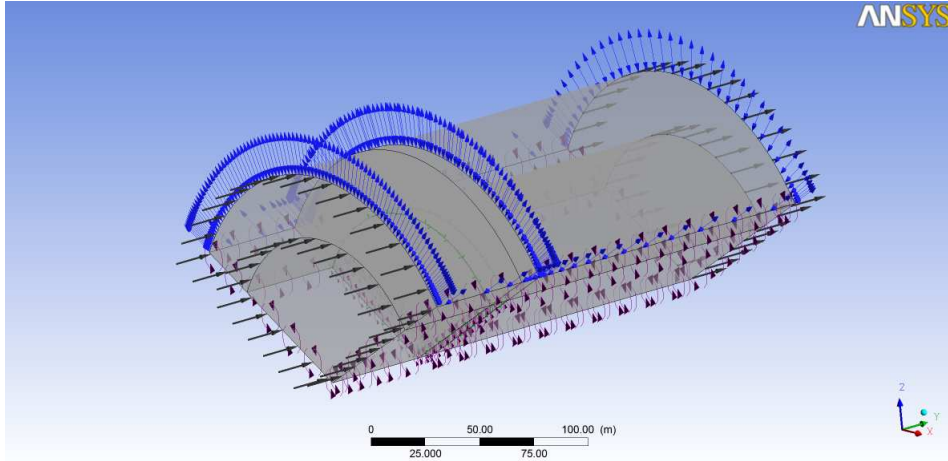


Figure 7.5.3: *Boundary conditions for the CFD simulation*

The total output power calculated by this CFD simulation is approximately 4.8 MW which is 5% less than the nominated output power of this wind turbine. The distribution of the tangential and thrust force along the blade is plotted and compared with those calculated by lifting line method. Apart from the deviation at the area near the tip, in most part of the blade, the two methods are in good agreement.

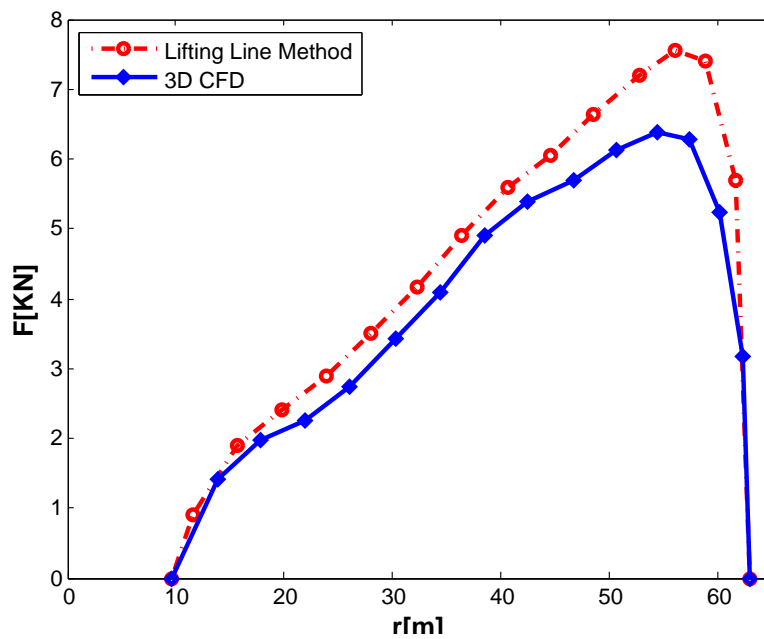


Figure 7.5.4: *Thrust force distribution along the blade, comparison of different methods*

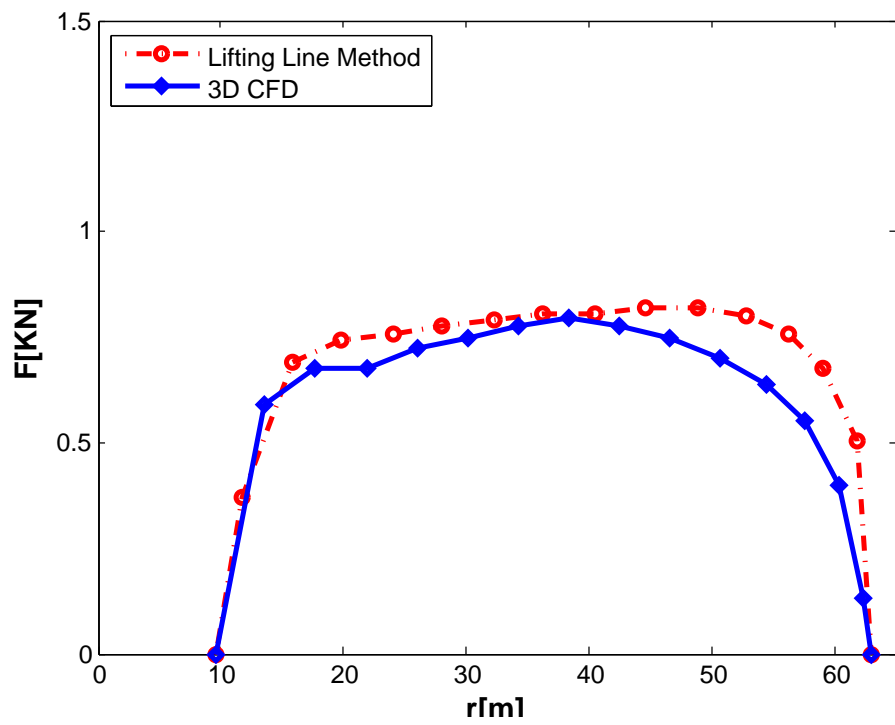


Figure 7.5.5: Tangential force distribution along the blade, comparison of different methods

8 Conclusion

In this report the helical vortex method is studied and applied to a standard wind turbine. This method has proved to have acceptable accuracy and since the computational time for this method is very low, it has the potential to be used as a designing tool. However this method requires 2D airfoil data of the profiles used for constructing the blade and the accuracy of this method cannot be better than its input. The second part of this report is devoted to address this problem where 2D CFD simulation with transitional turbulence modeling and the XFOIL program is used to acquire these data. Comparing these two methods showed that both methods are not accurate enough for predictions in after stall conditions. The XFOIL program, however, is much faster and easier than CFD simulation, and thus is coupled to the final lifting line program to predict the airfoil characteristics.

Bibliography

- [1] T. Abe K. Kondoh and Y. Nagano. “A new turbulence model for predicting fluid flow and heat transfer in separating and reattaching flows- 1. Flow field calculations”. In: *Int. J. Heat Mass Transfer* 37 (1994), pp. 139–151.
- [2] H.R Abedi. “Aerodynamic Loads On Rotor Blades”. MA thesis. Chalmers University of technology, 2011.
- [3] L. Davidson. “Prediction of the Flow Around an Airfoil Using a Reynolds Stress Transport Model”. In: *ASME Journal of Fluid Eng.* 117 (1995), pp. 50–57.
- [4] L. Davidson and B. Farhanieh. *CALC-BFC: A finite volume code employing collocated variable arrangement and cartesian velocity components for computation of fluid flow and heat transfer in complex three dimensional geometries.* report 92/4. Gothenburg,sweden: Chalmers university of technology,Department of applied mechanics,Thermo and fluid dynamics division, 1992.
- [5] Lars Davidson. *Fluid mechanics, turbulent flow and turbulence modeling.* Chalmers University of Technology. 2012.
- [6] T. B Gatski and Speziale C. G. “On explicit algebraic stress models for complex turbulent flows”. In: *J. Fluid Mech* 254 (1993), pp. 59–78.
- [7] K.Gersten H.Schlichting. *Boundary Layer Theory.* 8th. Berlin: Springer, 2000.
- [8] B. R. Jeng, Jr. T. G. Keith, and A. Aliakbarkhanafjeh. *Aerodynamic Analysis of a Horizontal Axis Wind Turbine by use of Helical Vortex Theory.* Technical report-NASA/CR-168054. Toledo, Ohio: Department of Mechanical Engineering University of Toledo, 1982.
- [9] Allen Plotkin Joseph Katz. *Low speed aerodynamics.* 2nd. New York: McGraw-Hill,Inc, 1991.
- [10] A.V. Menter F.R. Garbaruk and Y. Egorov. “Explicit Algebraic Reynolds Stress Models for Anisotropic Wall-Bounded Flows”. In: *3rd European Conference for Aero-Space Sciences* (2009).
- [11] F.R. Menter. “Correlation-Based Transition Modeling for Unstructured Parallelized Computational Fluid Dynamics Codes”. In: *AIAA Journal* 47.12 (2009).
- [12] F.R. Menter. “Two-equation eddy-viscosity turbulence models for engineering applications”. In: *AIAA Journal* 32 (1994), pp. 1598–1605.
- [13] S.B Pope. “A more general effective-viscosity hypothesis”. In: *J. Fluid Mech* 72 (1975), pp. 331–340.
- [14] A. M. Savill. “One-Point Closures Applied to Transition”. In: *Turbulence and Transition Modeling.* Ed. by M. Kluwer Hallbäck and Dordrecht. 1996, pp. 233–268.
- [15] A. M. Savill. “Some Recent Progress in the Turbulence Modeling of By-Pass Transition”. In: *Near-Wall Turbulent Flows.* Ed. by C. G. So R. M. C. Speziale and B. E. Launder. Elsevier, 1993.
- [16] G. B. Schubauer and P. S. Klebanoff. “Contribution on the Mechanics of Boundary Layer Transition”. In: *NACA TN 3489* (1995).
- [17] J.L Steger and D.S Chaussee. “Generation of body-fitted coordinates using Hyperbolic partial differential equations”. In: *SIAM J.Sci. stat. Comput.* 1.4 (1980), pp. 431–437.
- [18] S.L Tai C.H Yin and C.Y Soong. “A novel Hyperbolic Grid generation procedure with inherent adaptive dissipation”. In: *Journal of computational physics* 116 (1995), pp. 173–179.
- [19] D.B Taulbee. “An improved algebraic Reynolds stress model and corresponding nonlinear stress model”. In: *Phys. Fluids* (1992), pp. 2555–2561.
- [20] E.R. Van Driest and C.B. Blumer. “Boundary layer transition, Free stream turbulence and pressure gradient effects”. In: *AIAA journal* 1 (1963), pp. 1303–1306.
- [21] S. Wallin and A.V. Johansson. “A new explicit algebraic Reynolds stress model for incompressible and compressible turbulent flows”. In: *Journal of Fluid Mechanics* 403 (2000), pp. 89–132.
- [22] David C. Wilcox. *Turbulence modeling for CFD.* 3th. DCW Industries, 2006.